Acceleration of the hydrological cycle under global warming? An age-weighted regional water tagging approach

Jianhui Wei[1], Joel Arnault[2], Thomas Rummler[3], Benjamin Fersch[1], Zhenyu Zhang[4], Patrick Olschewski[5], Patrick Laux[6], Ningpeng Dong[7], Qianya Yang[8], Zikang Xing[9], Xin Li[9], Chuanguo Yang[10], Xuejun Zhang[11], Miaomiao Ma[7], Lu Gao[12], Ligang Xu[13], Zhongbo Yu[9], and Harald Günter Kunstmann[1]

[1]Karlsruhe Institute of Technology (KIT)
[2]Karlsruhe Institute of Technology KIT
[3]University of Augsburg
[4]Karlsruhe Institute of Technology KIT, Institute of Meteorology and Climate Research (IMK-IFU)
[5]Karlsruhe Institute of Technology - Campus Alpin
[6]Karlsruhe Institute of Technology
[7]China Institute of Water Resources and Hydropower Research
[8]Nanchang Institute of Technology
[9]Hohai University
[10]State Key Laboratory of Hydrology-Water Resources and Hydraulic Engineering, HoHai University, Nanjing 210098, PR China
[11]China Institue of Water Resources and Hydropower Research
[12]Fujian Normal University
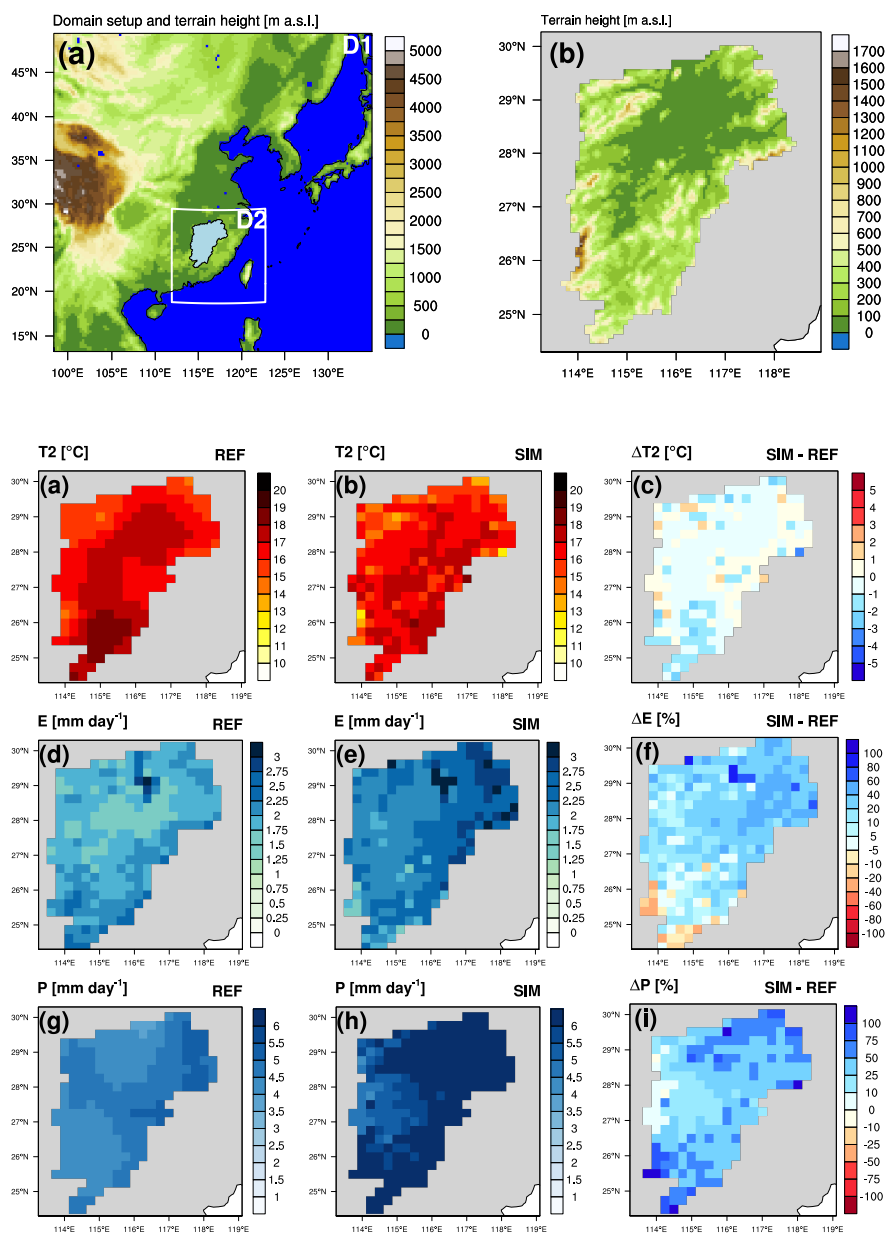[13]Nanjing Institute of Geography and Limnology, Chinese Academy of Sciences
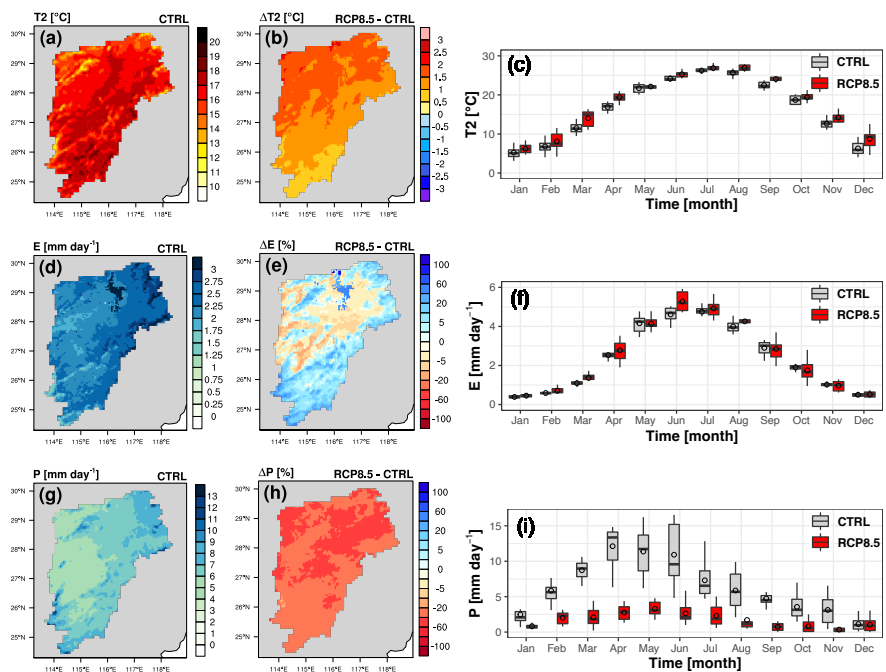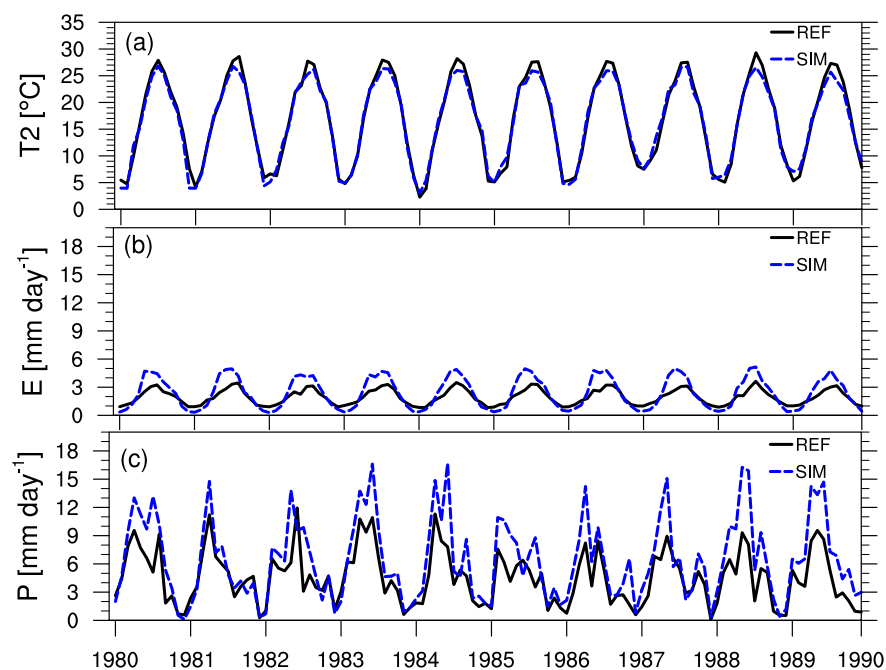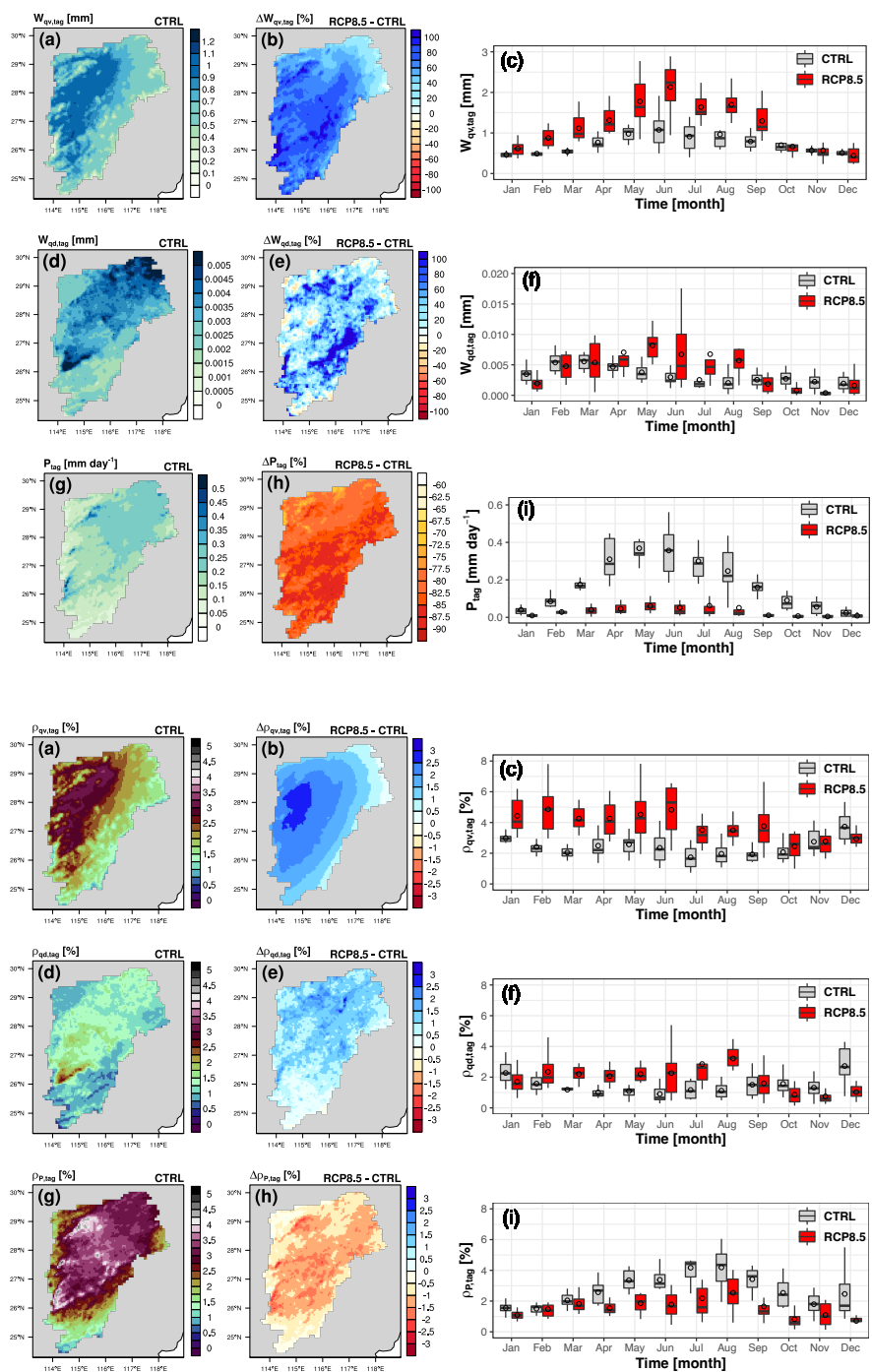
May 25, 2023

Abstract

Global warming is assumed to accelerate the global water cycle. However, quantification of the acceleration and regional analyses remain open. Accordingly, in this study we address the fundamental hydrological question: Is the water cycle regionally accelerating/decelerating under global warming? For our investigation we have implemented the age-weighted regional water tagging approach into the Weather Research and Forecasting WRF model, namely WRF-age, to follow the atmospheric water pathways and to derive atmospheric water residence times accordingly. Moreover, we have implemented the three-dimensional online budget analysis of the total, tagged, and aged atmospheric water into WRF-age to provide a prognostic equation of the atmospheric water residence times. The newly developed, physics-based WRF-age model is used to regionally downscale the reanalysis of ERA-Interim and the MPI-ESM Representative Concentration Pathway 8.5 scenario (RCP8.5) simulation exemplarily for an East Asian monsoon region, i.e., the Poyang Lake basin (the tagged moisture source area), for two 10-year slices of historical (1980-1989) and future (2040-2049) times. In comparison to the historical simulation, the future 2-meter temperature rises by +1.4 °C, evaporation increases by +6%, and precipitation decreases by -38% under RCP8.5 on average. In this context, global warming leads to regionally decreased residence times for the tagged water vapor by 8 hours and the tagged condensed moisture by 12 hours in the atmosphere, but increased transit times for the tagged precipitation by 4 hours over the land surface that is partly attributed to a slower fallout of precipitating moisture components in the atmosphere under global warming.

Hosted file

963123_0_art_file_11000404_rjth8b.docx available at https://authorea.com/users/619705/articles/644072-acceleration-of-the-hydrological-cycle-under-global-warming-an-age-weighted-regional-water-tagging-approach
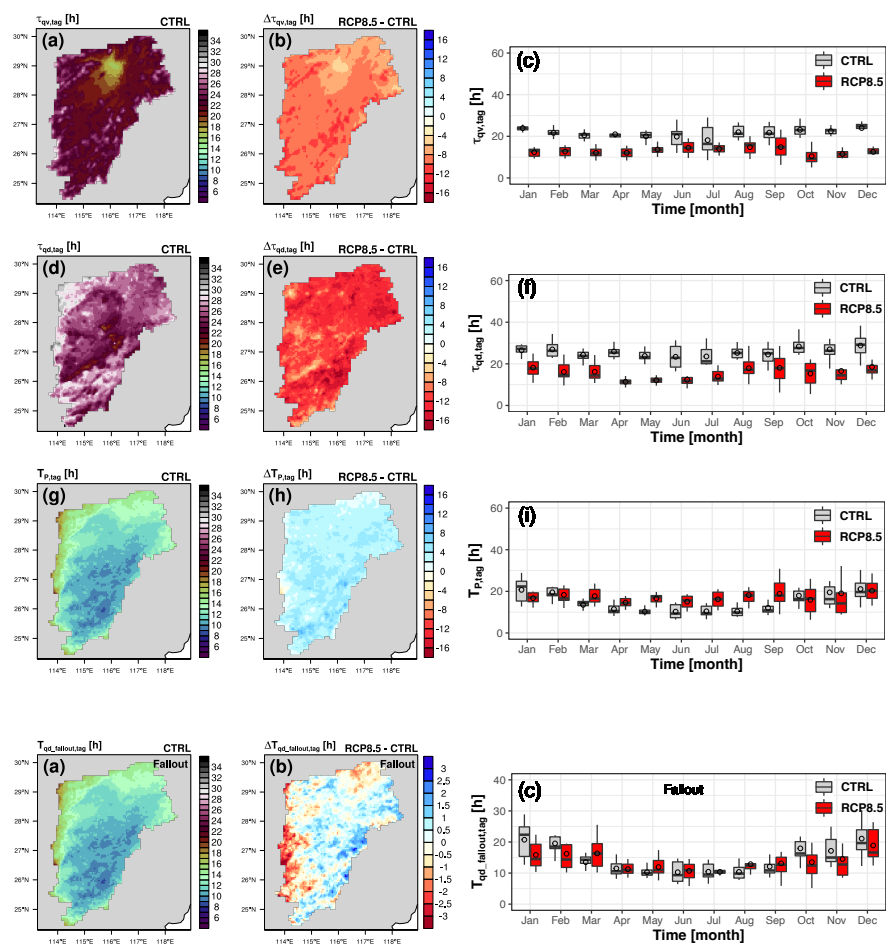
Hosted file

`963123_0_table_11000420_rgth8b.docx` available at https://authorea.com/users/619705/articles/644072-acceleration-of-the-hydrological-cycle-under-global-warming-an-age-weighted-regional-water-tagging-approach

1 **Acceleration of the hydrological cycle under global warming? An age-**

2 **weighted regional water tagging approach**

3 Jianhui Wei[1,*], Joël Arnault[1,2], Thomas Rummler[2], Benjamin Fersch[1], Zhenyu Zhang[1,2],

4 Patrick Olschewski[1], Patrick Laux[1,2], Ningpeng Dong[3], Qianya Yang[4], Zikang Xing[5], Xin

5 Li[6], Chuanguo Yang[7], Xuejun Zhang[8], Miaomiao Ma[8], Lu Gao[9], Ligang Xu[10], Zhongbo

6 Yu[7], and Harald Kunstmann[1,2]

7 [1]Institute of Meteorology and Climate Research (IMK-IFU), Karlsruhe Institute of Technology, Campus

8 Alpin, Garmisch-Partenkirchen, Germany

9 [2]Institute of Geography, Augsburg University, Augsburg, Germany

10 [3]Department of Water Resources, China Institute of Water Resources and Hydropower Research, Beijing,

11 China

12 [4]Nanchang Institute of Technology, Nanchang, China

13 [5]College of Hydrology and Water Resources, Hohai University, Nanjing, China

14 [6]College of Water Conservancy and Hydropower Engineering, Hohai University, Nanjing, China

15 [7]State Key Laboratory of Hydrology-Water Resources and Hydraulic Engineering, Hohai University,

16 Nanjing, China

17 [8]Research Center on Flood and Drought Disaster Reduction of the Ministry of Water Resources, China

18 Institute of Water Resources and Hydropower Research, Beijing, China

19 [9]Institute of Geography, Fujian Normal University, Fuzhou, China

20 [10]Key Laboratory of Watershed Geographic Science, Nanjing Institute of Geography and Limnology,

21 Chinese Academy of Sciences, Nanjing, China

22 [*]Corresponding author: Jianhui Wei (jianhui.wei@kit.edu) ORCID: 0000-0001-8609-9600

23 **Abstract**

24 Global warming is assumed to accelerate the global water cycle. However,

25 quantification of the acceleration and regional analyses remain open. Accordingly, in

26 this study we address the fundamental hydrological question: Is the water cycle

27 regionally accelerating/decelerating under global warming? For our investigation we

28 have implemented the age-weighted regional water tagging approach into the Weather

29 Research and Forecasting WRF model, namely WRF-age, to follow the atmospheric

30 water pathways and to derive atmospheric water residence times accordingly.

31 Moreover, we have implemented the three-dimensional online budget analysis of the

32 total, tagged, and aged atmospheric water into WRF-age to provide a prognostic

33 equation of the atmospheric water residence times. The newly developed, physics-

34 based WRF-age model is used to regionally downscale the reanalysis of ERA-Interim

35 and the MPI-ESM Representative Concentration Pathway 8.5 scenario (RCP8.5)

36 simulation exemplarily for an East Asian monsoon region, i.e., the Poyang Lake basin

37 (the tagged moisture source area), for two 10-year slices of historical (1980-1989) and

38 future (2040-2049) times. In comparison to the historical simulation, the future 2-meter

39 temperature rises by +1.4 °C, evaporation increases by +6%, and precipitation

40 decreases by -38% under RCP8.5 on average. In this context, global warming leads to

41 regionally decreased residence times for the tagged water vapor by 8 hours and the

42 tagged condensed moisture by 12 hours in the atmosphere, but increased transit times

43 for the tagged precipitation by 4 hours over the land surface that is partly attributed to a

44 slower fallout of precipitating moisture components in the atmosphere under global

45 warming.

46 **Keywords:** Atmospheric water residence times, acceleration of the atmospheric

47 hydrological cycle, the Weather Research and Forecasting model, age-weighted water

48 tagging approach, East Asian monsoon region

49 **Key Points**

50 • Age-weighted water tagging approach is implemented into WRF to derive the

51 atmospheric water residence time.

52 • 3-D online moisture budget analysis is extended in WRF for age-weighted

53 atmospheric water to provide a prognostic equation of the atmospheric residence

54 time.

55 • Global warming reduces the age of tagged water vapor and condensed moisture but

56 increases the age of tagged precipitation over the Poyang Lake basin.

1. Introduction

It is well-accepted that global warming has been accelerating the global hydrological cycle (Held & Soden, 2006; Huntington, 2006; Olmedo et al., 2022; Yu et al., 2020), as concluded from observational findings (Huntington, 2006), theoretical expectations (Held & Soden, 2006), and modeling studies (Allen & Ingram, 2002). Accordingly, at the regional scale, such acceleration modifies weather regimes and increases the number of hydrometeorological extremes (Ficklin et al., 2019; Giorgi et al., 2011; Gu et al., 2023), thereby increasing the complexity of water resources management (Ficklin et al., 2022; Vahmani et al., 2022). Furthermore, continuous global warming in the future could also trigger multiple climate tipping points, which makes the changes (here, acceleration/deceleration) of the hydrological cycle at the regional scale and their associated impacts more complex (McKay et al., 2022; Blöschl et al., 2019; Lenton et al., 2008; Olschewski et al., 2023). Therefore, the understanding of regional hydrological cycle responses to global warming is fundamental to risk mitigation.

To quantify the acceleration/deceleration of the hydrological cycle, two types of approaches are often used: analytical methods with multiple datasets and numerical models with water-tracking techniques. For analytical methods, multiple indices are proposed to investigate the changes in the intensity of water fluxes in the hydrological cycle under global warming. For example, Giorgi et al. (2011) introduced the hydroclimatic intensity (HY-INT) index that synthesizes two metrics of precipitation intensity and dry spell length, with applications at regional and global scales (Giorgi et al., 2014; Mohan & Rajeevan, 2017). Huntington et al. (2018) presented the Water Cycle Intensity (WCI), which takes precipitation and actual evapotranspiration into

80 account, for quantifying the intensity of the hydrological cycle from a landscape point of

81 view across multiple temporal scales. Recently, Ficklin et al. (2019) integrated

82 precipitation surplus and evaporative demand, namely, the Surplus Deficit Intensity

83 Index (SDI), to quantify hydrologic intensification by additionally accounting for changed

84 atmospheric water demand under global warming. However, these indices can focus

85 solely on changes in fluxes of water between terrestrial and atmosphere, which neglects

86 atmospheric moisture transport, and in this case the acceleration/deceleration of the

87 hydrological cycle can only be inferred.

88   A numerical model with water tracking techniques is an additional and more

89 straightforward way to derive residence times of water in the atmosphere, i.e., a

90 measure of the speed of the atmospheric hydrological cycle, and thereby evaluate

91 changes in the speed and potential acceleration/deceleration of the hydrological cycle

92 (van der Ent & Tuinenburg, 2017; Gimeno et al., 2021; Läderach & Sodemann, 2016;

93 Trenberth, 1998; Tuinenburg & van der Ent, 2019; Wang et al., 2018; Wei et al., 2016).

94 Here, the atmospheric water residence time is defined as the time between the original

95 evaporation and the return of its respective water masses to the land surface as

96 precipitation. Technically, moisture/particle tracking in numerical atmospheric models

97 allows to characterize the pathways of evaporated and/or precipitating water with the

98 consideration of atmospheric moisture transport and to diagnose the residence times of

99 water vapor in the atmosphere (Bosilovich, 2002; Bosilovich et al., 2005; van der Ent et

100 al., 2014; Läderach & Sodemann, 2016; Numaguti, 1999; Stohl & James, 2004; Wei et

101 al., 2016). For example, Stohl & James (2004) implemented a Lagrangian analog to the

102 Eulerian water budget analysis into the Lagrangian particle dispersion FLEXPART

103   model to derive the residence times in the total atmospheric column out of the

104   meteorological analysis. Läderach & Sodemann (2016) further refined Lagrangian

105   moisture source diagnostics and highlighted that simplified representations of moisture

106   transport and precipitation processes in the tracking models lead to an overestimation of

107   atmospheric moisture residence time globally. However, in FLEXPART, only the rate of

108   change for the difference between evaporation and precipitation is diagnosed along

109   trajectories, so that the respective impacts of evaporation and precipitation changes on

110   the atmospheric moisture residence time cannot be disentangled (van der Ent &

111   Tuinenburg, 2017). Recently, Tuinenburg & van der Ent (2019) extended the quasi-

112   isentropic back-trajectory method of Dirmeyer & Brubaker (2007) to derive the

113   probability density function of residence time of land evaporation on a global scale. Still,

114   their model does not account for the vertical wind fields and neglects the vertical

115   redistribution of the tracked parcel of water, which might introduce uncertainties in the

116   derived patterns of the atmospheric residence time of water (Bosilovich, 2002;

117   Goessling & Reick, 2013).

118   In addition to the Lagrangian framework, several Eulerian modeling frameworks

119   have been proposed to estimate the residence time of atmospheric water in an offline

120   calculation mode (van der Ent et al., 2014; Wang et al., 2018; Yoshimura et al., 2004).

121   For example, the dynamic recycling model DRM (Wang et al., 2018) and the water

122   account model WAM-2 Layers (Benedict et al., 2021; van der Ent et al., 2014; van der

123   Ent et al., 2010; Wang-Erlandsson et al., 2018) take atmospheric analyses or model

124   outputs, such as horizontal wind fields, specific humidity, surface pressure, precipitation,

125   and evaporation, as their model inputs for forward-tracking of evaporation and

126   backward-tracking of precipitation. Accordingly, the atmospheric moisture residence

127   time increases linearly with time and is weighted by the updated tracked moisture during

128   model iteration at each time step. However, the two-dimensional field assumption does

129   not allow to account for three-dimensional effects such as wind shear and moist

130   convection (Goessling and Reick, 2013; van der Ent et al., 2013), and simple averaging

131   of estimates for different length scales and timescales may overlook the heterogeneity

132   of the land surface and the temporal variability (Bosilovich & Schubert, 2001; Trenberth,

133   1999).

134   To explicitly resolve the thermodynamical and precipitating processes and thus to

135   more realistically estimate the atmospheric moisture residence time, atmospheric online

136   models with the implementation of three-dimensional numerical water tagging

137   approaches have been used (Bosilovich et al., 2005; Bosilovich & Schubert, 2002; Wei

138   et al., 2016). In the last years, the numerical water tagging approaches have been

139   elaborated within regional climate models to investigate the moisture sources for

140   precipitation extremes and monsoon systems (Arnault et al., 2016; Dominguez et al.,

141   2016; Knoche & Kunstmann, 2013; Sodemann et al., 2009; Winschall et al., 2014).

142   Moreover, an "age-weighted" regional water tagging approach has been developed and

143   successfully implemented in one regional climate model (Wei et al., 2016). This

144   implementation allows for calculating residence times of atmospheric water states of

145   matter (i.e., different types of hydrometeors) and for diagnosing the speed of the

146   atmospheric branch of the hydrological cycle, which can be used to quantitatively

147   assess the regional effects of global warming-induced acceleration of the hydrological

148   cycle (Held & Soden, 2006; Huntington, 2006; Olmedo et al., 2022; Yu et al., 2020) in

149   more detail. Because of these advanced features, the RCM-derived highly accurate

150   three-dimensional magnitude, location, and residence time of tagged atmospheric water

151   states of matter have been often used to guide the future improvements of analytical

152   methods for precipitation recycling studies, such as DRM (Dominguez et al., 2016) and

153   WAM-2 Layer (van der Ent et al., 2013).

154   The land surface is characterized as highly heterogeneous concerning land cover,

155   terrain height, and soil texture (Yates et al., 2003), and thereby interactions between the

156   land surface and atmosphere are highly non-linear across scales (Betts et al., 1996;

157   Wulfmeyer et al., 2018; Zhang et al., 2021). Over the last two decades, one of the

158   Global Land Atmosphere System Study (GLASS) working groups (Hurk et al., 2011),

159   namely, local coupling (LoCo) of land-atmosphere, promotes to develop processes-level,

160   quantifiable metrics to diagnose the coupling among the land, planetary boundary layer,

161   and precipitation (Santanello et al., 2018). However, the existing LoCo metrics listed in

162   Santanello et al. (2018) have limited applicability in terms of investigated processes and

163   temporal scales. Specifically, the process-based LoCo metrics summarized by

164   Santanello et al. (2018), e.g., the concept of vector representation of heat and moisture

165   budgets in the form of mixing diagrams (Milovac et al., 2016), do not apply to account

166   for cloud formation and precipitating effect, and are not able to distinguish the local

167   coupling of one specific region from other regions. To tackle the limitations of the

168   existing LoCo metrics, the RCM-based regional water tagging approach is capable to

169   quantify local land-atmosphere interactions by explicitly following atmospheric pathways

170   of the water evaporated from a pre-defined region until it precipitates.

171   Using a RCM-based regional water tagging approach, the present study aims to

172 address our hydrologically fundamental research question "Is the hydrological cycle

173 regionally accelerating/decelerating under climate change?", which has been ranked as

174 the first out of the twenty-three unsolved problems in hydrology identified by the

175 community process in 2018 (Blöschl et al., 2019). In particular, we present the newly

176 developed WRF-age modeling system, that is the state-of-the-art Weather Research

177 and Forecasting WRF model enhanced with the implementation of the age-weighted

178 regional water tagging approach. For the case-study application, we choose to simulate

179 and compare future and historical periods for the southeastern region of China, a region

180 characterized by a monsoonal precipitation regime with a dry season during the winter

181 months and a wet season during the summer months. It is reported that global warming

182 may shift the position of this East Asian monsoonal circulation (Li et al., 2010; Li et al.,

183 2023), which potentially generates droughts or floods in areas where this usually does

184 not happen, thus affecting local economy (Hu et al., 2016). Recent studies also highlight

185 that economic losses in China caused by warming-induced weather and climate

186 extremes such as droughts, floods, and compound events might double between the

187 1.5 °C and 2.0 °C warming (Hao, 2022; Liu et al., 2022; Su et al., 2018).

188   The objectives of the present study are (1) to implement the age-weighted

189 regional water tagging approach of Wei et al. (2016) and the three-dimensional online

190 atmospheric water budget analysis of Arnault et al. (2016) into the Weather Research

191 and Forecasting WRF modeling system, namely, the WRF-age, (2) to apply the WRF-

192 age model to the Poyang Lake basin in the East Asian monsoon region for two 10-year

193 slices of historical and future-warming times, and (3) to quantify to what extent the

194 regional atmospheric hydrological cycle is accelerated/decelerated under global

195 warming.

2. Model and methodology

2.1. WRF with the age-weighted regional water tagging approach

198 The Weather Research and Forecast WRF model version 3.6.1 (Skamarock et

199 al., 2008) is extended and employed for our accelerated/decelerated atmospheric

200 hydrological cycle modeling study. WRF is a limited-area mesoscale model that

201 simulates a coupled, nonlinear system of the soil, the vegetation, and the atmosphere.

202 The WRF model has been employed for applications of, short-term weather forecasting

203 (Gao et al., 2022; Yang et al., 2021), seasonal forecasts (Mori et al., 2020; Siegmund et

204 al., 2015), historical climate simulations (Fersch & Kunstmann, 2014; Shang et al.,

205 2022), and future climate projections (Wagner et al., 2013; Warrach-Sagi et al., 2013).

206 An evaporation tagging algorithm has been implemented in the WRF model

207 version 3.5.1 by Arnault et al. (2016), with numerous applications for regions in Europe

208 (Arnault et al., 2019), Africa (Arnault et al., 2021), and China (Shang et al., 2022; Zhang

209 et al., 2019, 2022). This evaporation tagging algorithm is adapted to the WRF model

210 version 3.6.1 used in this study, and further enhanced with the age-weighted

211 evaporation tagging approach for regional climate models given by Wei et al. (2016).

212 For the implementation of the age-weighted regional water tagging approach into the

213 so-called WRF-age model, we closely follow our previous study in Wei et al. (2016). The

214 age-weighted regional water tagging approach and the implementation strategy into

215 regional climate models from Wei et al. (2016) has originally been developed with the

216   Fifth-Generation Pennsylvania State University/National Center for Atmospheric

217   Research Mesoscale Model (MM5) version 3.5 (Dudhia, 1993; Grell et al., 1994).

218   The implementation of the age-weighted water tagging approach in WRF-age is

219   summarized in three steps:

220   (1) Tagged evaporated water E_{tag} is calculated from a pre-defined moisture

221   source area of the land surface by implementing a mask MASK$_{tag}$ in the lower boundary

222   condition of WRF;

$$E_{tag} = E \times \text{MASK}_{tag} \tag{1}$$

$$\text{MASK}_{tag} = \begin{cases} 1 & \text{for moisture source area} \\ 0 & \text{otherwise} \end{cases} \tag{2}$$

223   (2) The tagged water (Equation 3) and the age-weighted tagged water (Equation

224   4) are tracked until it returns to the land surface as precipitation by following the

225   atmospheric water pathways. For this implementation, two additional equation sets for

226   the tagged water states of matter $q_{k,tag}$ (kg kg^{-1}) and the age-weighted water states of

227   matter $\tilde{q}_{k,tag}$ (kg kg^{-1} s), describing three-dimensional grid-scale transport, horizontal *H*

228   and vertical *V* subgrid-scale transport due to turbulence and diffusion *F*, phase change

229   *C*, and the downward transport (namely, fallout) of precipitating water components *P*,

230   are added to WRF-age. The subscript *k* denotes different types of hydrometeors.

$$\frac{\partial}{\partial t}\left(\mu \cdot q_{k,tag}\right)$$

$$= -\underbrace{\left[\frac{\partial\left(\mu \cdot u \cdot q_{k,tag}\right)}{\partial x} + \frac{\partial\left(\mu \cdot v \cdot q_{k,tag}\right)}{\partial y} + \frac{\partial\left(\mu \cdot (g \cdot w - \Phi_x \cdot u - \Phi_y \cdot v) \cdot q_{k,tag}\right)}{\partial \eta}\right]}_{\text{Grid-scale transport}} \tag{3}$$

$$+ \underbrace{\mu \cdot \left(F_{q_{k,tag}}^H + F_{q_{k,tag}}^V\right)}_{\text{Subgrid-scale transport}} + \underbrace{\mu \cdot C_{q_{k,tag}}}_{\text{Phase change}} + \underbrace{\mu \cdot P_{q_{k,tag}}}_{\text{Fallout}}$$

$$\frac{\partial}{\partial t}\left(\mu \cdot \tilde{q}_{k,tag}\right)$$

$$= -\underbrace{\left[\frac{\partial\left(\mu \cdot u \cdot \tilde{q}_{k,tag}\right)}{\partial x} + \frac{\partial\left(\mu \cdot v \cdot \tilde{q}_{k,tag}\right)}{\partial y} + \frac{\partial\left(\mu \cdot (g \cdot w - \Phi_x \cdot u - \Phi_y \cdot v) \cdot \tilde{q}_{k,tag}\right)}{\partial \eta}\right]}_{\text{Grid-scale transport}} \tag{4}$$

$$+ \underbrace{\mu \cdot \left(F^H_{\tilde{q}_{k,tag}} + F^V_{\tilde{q}_{k,tag}}\right)}_{\text{Subgrid-scale transport}} + \underbrace{\mu \cdot C_{\tilde{q}_{k,tag}}}_{\text{Phase change}} + \underbrace{\mu \cdot P_{\tilde{q}_{k,tag}}}_{\text{Fallout}} + \underbrace{S_{\tilde{q}_{k,tag}}}_{\text{Advancing time}}$$

231   Here $\mu = P_{hs} - P_{ht}$ (Pa) represents the difference between the hydrostatic pressures at

232   the top P_{ht} and surface P_{hs} of the model, which represents the mass of the dry air per

233   unite area within the modeled atmospheric column. x (m) and y (m) denote the two

234   horizontal coordinates. η (-) is the terrain-following hydrostatic pressure (mass) vertical

235   coordinate. u (m s^{-1}), v (m s^{-1}), and w (m s^{-1}) are the two horizontal and vertical wind

236   components. Φ (m^2 s^{-2}) is the geopotential and g (m s^{-2}) is the acceleration of gravity.

237   (3) Time weight information is included to the age-weighted tagged water due to

238   atmospheric transport and phase change processes, in order to advance time for the

239   age-weighted tagged water $\tilde{q}^{t+1}_{k,tag}$ at each model iteration as

$$\tilde{q}^{t+1}_{k,tag} = \tilde{q}^t_{k,tag} + \left(q^{t+1}_{k,tag} - q^t_{k,tag}\right) \times \Delta T, \tag{5}$$

240   where ΔT (s) denotes the model time step length and $\tilde{q}^t_{k,tag}$ denotes the preliminary

241   age-weighed tagged moisture components from the previous model time step t due to

242   time-weighted atmospheric transport and phase change.

2.2. Extension of the online budget analysis for age-weighted tagged water

244   In this study, we further extend the three-dimensional online atmospheric water

245   budget analysis of Arnault et al. (2016) for age-weighted tagged water, thereby

246   providing a prognostic equation of the residence time of state variables in the

247   atmospheric hydrological cycle.

248   The concept of the online budget analysis of atmospheric water states of matter

249   is to compute the physical and dynamical tendencies of the model time step during

250   model integration (Langhans, Fuhrer, et al., 2012). Such online budget analysis has

251   been implemented into different regional climate models, such as the non-hydrostatic

252   Consortium for Small-Scale Modeling (COSMO) model (Langhans, Schmidli, et al.,

253   2012), the MM5 model (Braun, 2006), and the WRF model (Fita et al., 2019), for

254   disentangling the precipitation generation mechanisms. In addition to the original

255   atmospheric water states of matter, this approach has been extended by Arnault et al.

256   (2016) for tagged atmospheric water states of matter (Equation 6) to understand the

257   scale-dependency of regional precipitation recycling.

$$
\left(dz \cdot \rho_d \cdot q_{k,tag}\right)_t = \underbrace{dz \cdot \rho_d \cdot \mu^{-1} \cdot \left[-\frac{\partial\left(\mu \cdot u \cdot q_{k,tag}\right)}{\partial x} - \frac{\partial\left(\mu \cdot v \cdot q_{k,tag}\right)}{\partial y} + \mu \cdot F^H_{q_{k,tag}} \right]}_{\text{Horizontal transport}}
$$

$$
+ \underbrace{dz \cdot \rho_d \cdot \mu^{-1} \cdot \left[-\frac{\partial\left(\mu \cdot (g \cdot w - \Phi_x \cdot u - \Phi_y \cdot v) \cdot \tilde{q}_{k,tag}\right)}{\partial \eta} + \mu \cdot F^V_{q_{k,tag}} \right]}_{\text{Vertical transport}} \tag{6}
$$

$$
+ \underbrace{dz \cdot \rho_d \cdot C_{q_{k,tag}}}_{\text{Phase change}} + \underbrace{dz \cdot \rho_d \cdot P_{q_{k,tag}}}_{\text{Fallout}}
$$

258   where dz (m) is the height step for a given model layer and ρ_d is the density of dry air.

259   In our WRF-age modeling environment, we use the online budget analysis of

260   Equation 6 for tagged water and further extend this online budget analysis for age-

261   weighted water. For this new extension, analogously to the implementation of the online

262   budget analysis for tagged water in regional climate models described in Arnault et al.

263   (2016), new variables representing budgets of the age-weighted tagged atmospheric

264 water states of matter are defined, and new diagnostic equations of Equation 7

265 integrating instantaneous values of the defined variables over space, height, and time

266 are formulated in the source code of WRF. Terms of Equations 6 and 7 are integrated

267 online at the time step of the model to provide a budget of tagged and age-weighted

268 tagged atmospheric water states of matter, thereby allowing to calculate the

269 atmospheric transit times of water.

$$
(dz \cdot \rho_d \cdot \tilde{q}_{k,tag})_t = \underbrace{dz \cdot \rho_d \cdot \mu^{-1} \cdot \left[-\frac{\partial(\mu \cdot u \cdot \tilde{q}_{k,tag})}{\partial x} - \frac{\partial(\mu \cdot v \cdot \tilde{q}_{k,tag})}{\partial y} + \mu \cdot F^H_{\tilde{q}_{k,tag}} \right]}_{\text{Horizontal transport}}
$$

$$
+ \underbrace{dz \cdot \rho_d \cdot \mu^{-1} \cdot \left[-\frac{\partial(\mu \cdot (g \cdot w - \Phi_x \cdot u - \Phi_y \cdot v) \cdot \tilde{q}_{k,tag})}{\partial \eta} + \mu \cdot F^V_{\tilde{q}_{k,tag}} \right]}_{\text{Vertical transport}} \qquad (7)
$$

$$
+ \underbrace{dz \cdot \rho_d \cdot C_{\tilde{q}_{k,tag}}}_{\text{Phase change}} + \underbrace{dz \cdot \rho_d \cdot P_{\tilde{q}_{k,tag}}}_{\text{Fallout}} + \underbrace{S_{\tilde{q}_{k,tag}}}_{\text{Advancing time}}
$$

2.3. Quantification of the atmospheric water pathways

270

271 The model extensions of section 2.1 and section 2.2 allow us to derive two

272 categories of metrics to quantitatively understand the atmospheric water pathways,

273 which are then employed to assess to what extent the regional atmospheric water cycle

274 is accelerated/decelerated under global warming.

275 The contribution ratio ρ_W (%) is used to evaluate the strength of the land-

276 atmosphere interaction. It quantifies to what extent the tagged water states of matter

277 W_{tag} originating from a pre-defined moisture source region contributes to the total

278 (original) water states of matter W in the atmospheric hydrological cycle:

$$
\rho_W = W_{tag}/W_{total} \times 100 \qquad (8)
$$

279   W denotes arbitrary column-integrated variables, such as, water vapor q_v, condensed

280   atmospheric moisture q_d.

281   The atmospheric residence time τ_W (h) is defined as the age of tagged water

282   since its source (hereafter referred to as the age of water), evaluated with the ratio

283   between an age-weighted tagged variable and the corresponding tagged variable as

$$\tau_{W,tag} = \widetilde{W}_{tag}/W_{tag} \tag{9}$$

284   where $\widetilde{W}_{tag}$ denotes arbitrary column-integrated age-weighted tagged variables.

285   We further define the atmospheric transit time $T_{W,tag}$ (h) as the age of tagged

286   water since its source originating from a particular physical or dynamical process *pro*

287   (hereafter referred to as the age of water in flux), such as fallout and precipitation.

$$T_{W\_pro,tag} = \widetilde{W}_{pro,tag}/W_{pro,tag} \tag{10}$$

288

289   **3. The experimental design**

290   **3.1. Study area**

291   This WRF-age modeling study focuses on the Poyang Lake basin (Figure 1a)

292   with a spatial coverage of the basin of around 162,000 km^2 (Wei et al., 2021). The

293   topography of the basin varies from around 2000 m in the south to 50 m around the lake

294   area (Figure 1b). Poyang Lake, located in the northern part of the basin (29°N, 116°E),

295   is the largest freshwater lake in China. In a hydrological normal year, the area of the

296   lake is approximately 3,500 km^2 and the average depth of the lake is approximately 8.4

297   m (Feng et al., 2011). The land use in the Poyang Lake basin consists of forest (46%),

298   shrubland (25%), cropland (25%), and small areas of pasture, urban, and open water

299   (4%) (Ye et al., 2011; Zhang et al., 2014). The climate of the basin is categorized as a

300   humid subtropical climate and has a strong seasonality of hot humid summers and cool

301   dry winters (Wagner et al., 2016), which is mainly controlled by the East Asian monsoon

302   (Ding & Chan, 2005; Xing et al., 2022; Zhang et al., 2011). The rainy season of the

303   basin ranges from April to June and the summer is from June to August (Zhang et al.,

304   2016). The mean annual basin-averaged 2-meter air temperature is around 17.5 °C,

305   evaporation and precipitation are around 900 mm year^{-1} and 1680 mm year^{-1},

306   respectively (Li & Zhang, 2011; Wei et al., 2015; Xing et al., 2022).

307   **3.2. Domain setup and model configuration**

308   For the domain setup and general model configuration of the newly developed

309   WRF-age model, we closely follow the selection as chosen by Wei et al. (2015) and

310   Wagner et al. (2016). A nested two-domain setup (Figure 1a) is used in this study. The

311   first domain (D1) has a horizontal resolution of 30 km and an uneven vertical

312   discretization of 38 layers up to 50 hPa for the atmosphere. The second domain (D2),

313   centered over the Poyang Lake basin (Figure 1b), has a horizontal resolution of 5 km

314   and 38 vertical layers of the atmosphere.

315   Table 1 lists the physical schemes of the WRF-age model applied in this study

316   for both D1 and D2. They consist of the Dudhia scheme (Dudhia, 1989) for calculating

317   shortwave radiation, the Rapid Radiation Transfer Model (RRTM) (Mlawer et al., 1997)

318   for calculating longwave radiation, the WRF Single-Moment five-class scheme (WSM5)

319   microphysics scheme (Hong et al., 2004), the Yonsei University (YSU) planetary

320   boundary layer scheme (Hong et al., 2006), the Revised MM5 Monin-Obukhov surface

321   layer scheme (Jiménez et al., 2012), the NOAH land surface model (Chen & Dudhia,

322 2001). For parameterizing cumulus, the Betts-Miller-Janjic (BMJ) scheme (Betts, 1986;

323 Betts & Miller, 1986; Janjić, 2002) is applied only for the outer domain D1. The model

324 setup and the physical schemes selected in this study have been intensively evaluated

325 and widely used in our previous studies of regional climate modeling for the Poyang

326 Lake basin (Wagner et al., 2013; Wagner et al., 2016; Wei et al., 2015, 2016).

327 For the WRF-age setup, the moisture source area of the Earth's land surface

328 focused on in this study is the Poyang Lake basin (light blue shaded area in Figure 1a),

329 from which the evaporated water is "tagged, tracked, and aged" when entering the

330 atmosphere. To separate the moisture source of the Poyang Lake basin from the

331 surrounding, a pre-defined mask (with values of 1 for the Poyang Lake basin and of 0

332 for otherwise, Equations 1 and 2) is added into the static boundary condition of WRF-

333 age for D2. Then, the tagged and age-weighted water undergo the same dynamic and

334 physical processes of the atmosphere as the original atmospheric water states of matter,

335 until they return to the land surface of D2 as tagged and age-weighted tagged

336 precipitation or leave the D2 model domain.

337 **3.3. Simulation protocol**

338 In this study, two regional dynamical downscaling simulations using the newly

339 developed WRF-age model are conducted: (1) a control simulation for historical periods

340 (CTRL) and (2) a warming scenario simulation under Representative Concentration

341 Pathway 8.5 for future periods (RCP8.5), which corresponds to the atmospheric carbon

342 dioxide concentration being in the range of 851-1379 ppm by 2100. All two simulations

343 are carried out for the East Asian monsoon region for an 11-year slice. The first year of

344 two simulations is selected as the model spin-up time and the remaining 10 years of the

345 simulations are used for the warming-induced acceleration/deceleration analysis.

346   For the CTRL simulation, the initial and lateral boundary conditions to drive the

347 WRF-age model are taken from the European Centre for Medium Range Weather

348 Forecasts Interim reanalysis (Dee et al., 2011). The CTRL simulation is initialized on

349 January 1st, 1979 at 0000 UTC and covers the historical period 1979-1989. For the

350 RCP8.5 simulation, the Max-Planck-Institute Earth System Model (MPI-ESM) RCP8.5

351 scenario (Giorgetta et al., 2013) is dynamically downscaled using WRF-age for the

352 future period 2039-2049.

353   Regarding the selection of the emission scenario RCP8.5, this is because that,

354 for our investigation future period 2040-2049, the changes in the projected temperature

355 and precipitation over South China under RCP4.5 follows those under RCP8.5, with

356 relatively fewer deviations in comparison with these during far future periods, e.g., 2090-

357 2100 (Gu et al., 2015). On the other hand, our selection of the high-emission RCP8.5

358 warming scenario referred to as "business-as-usual" facilitates the elaboration of the

359 accelerated atmospheric hydrological cycle under global warming.

360   MPI-ESM is selected because the changes in the projected precipitation and

361 temperature over South China by the MPI models are most similar to those derived from

362 the multiple model ensemble of CMIP5 (Gu et al., 2015), and latest CMIP6 models (You

363 et al., 2021; Zhang et al., 2022). Therefore, it is expected that our WRF-age downscaled

364 MIP-ESM future projection over the Poyang Lake basin is in agreement with the robust

365 regional climate change signals derived from the multiple model ensemble.

366   To quantitively assess the warming-induced alternations of the regional

367   atmospheric water cycle, we denote

$$\Delta(\cdot) = (\cdot)_{\text{RCP8.5}} - (\cdot)_{\text{CTRL}} \qquad (11)$$

368   where subscripts "RCP8.5" and "CTRL" indicate the values of an arbitrary quantity in

369   parentheses during the future warming period and the historical period.

3.4. Reference data and evaluation strategy

371   To evaluate the performance of the basic WRF model in reproducing the

372   historical climate of the study region, the simulated 2-meter air temperature $T2$,

373   evaporation E, and precipitation P from the CTRL simulation are compared to gridded

374   reference datasets. For $T2$ and P, the CN05.1 product released by China

375   Meteorological Administration is used. It provides daily gridded temperature and

376   precipitation estimates over China since 1961 at a horizontal resolution of 0.25° (Wu &

377   Gao, 2013). CN05.1 is derived by spatially interpolating records collected from around

378   2416 meteorological stations in China. For E, the satellite- and reanalysis-based Global

379   Land Evaporation Amsterdam Methodology (GLEAM) version 3.6a product is chosen.

380   GLEAM provides daily gridded global evaporation estimates for the period 1980-2021 at

381   a 0.25° × 0.25° spatial resolution (Martens et al., 2017). Relative to the previous version

382   3.3, the upgraded version 3.6a is derived by additionally merging the latest reanalysis

383   ERA5 and by updating to the latest version of input data sets (e.g., precipitation, soil

384   moisture) using the revised approaches for calculating evaporative stress, optimizing

385   drainage, and assimilating soil moisture (Martens et al., 2017). The reference datasets

386   selected in this study have been widely used for validating regional climate simulations

387   (e.g., Shang et al., 2022) and for studying climate changes (e.g., Shang et al., 2021) in

388   East Asian monsoon regions.

389   For comparison of the simulations to the reference data, the bilinear interpolation

390   method is employed to remap the simulated variables of the WRF grids to the

391   respective reference data grids. Three statistical metrics, namely, mean error *ME*, mean

392   relative error *MRE* (%), and Pearson's correlation coefficient *r* (-) with a calculated *p*-

393   value (here the significance level of 99% is employed), are used to quantify the

394   performance of the WRF model in terms of reproducing spatial patterns and temporal

395   variations of *T2*, *E*, and *P* of the reference:

$$ME = \sum_{t=1}^{t=N}(SIM_t - REF_t) \tag{12}$$

$$MRE = \frac{\sum_{t=1}^{t=N}(SIM_t - REF_t)}{\sum_{t=1}^{t=N} REF_t} \times 100\% \tag{13}$$

$$r = \frac{\sum_{t=1}^{t=N}(SIM_t - \overline{SIM})(REF_t - \overline{REF})}{\sqrt{\sum_{t=1}^{t=N}(SIM_t - \overline{SIM})^2}\sqrt{\sum_{t=1}^{t=N}(REF_t - \overline{REF})^2}} \tag{14}$$

396   where SIM_t and REF_t denote the simulated and reference variable at the tth time step of

397   evaluation, respectively. *N* is the total number of time steps of evaluation. $\overline{SIM}$ and $\overline{REF}$

398   denote the spatial (temporal) mean of the simulated and reference variables for the

399   evaluation of spatial pattern (temporal variation), respectively.

400   **4. Results and discussion**

401   In this section, we investigate the warming-altered regional water cycle by comparing

402   the WRF-age downscaled RCP8.5 simulation with CTRL simulation, concerning land

403 surface process, atmospheric water pathways, land-atmosphere interactions, and

404 atmospheric water residence times.

405 **4.1. Evaluation of simulated T2, E, and P**

406 Figure 2 shows the spatial distributions of *T2*, *E,* and *P* derived from the

407 reference datasets (left column) and the WRF simulation (middle column) for the

408 Poyang Lake basin averaged for 1980-1989, and the corresponding differences in the

409 spatial patterns (right column). Figure 3 compares the monthly variations of the basin-

410 averaged, simulated *T2*, *E*, and *P* to the reference data from 1980 to 1989.

411 For *T2*, the observed pattern of higher temperatures over the central and

412 southern parts of the basin (Figure 2a) is well reproduced by the simulation (Figure 2b),

413 with very minor cold biases (*ME* = -0.4 °C, in Figure 2c). The monthly variation in the

414 simulated basin-averaged *T2* matches well with the variation of the observation (*r* =

415 0.99; *p*-value < 0.01), although slightly cold biases over the basin are found in summer

416 (Figure 3a).

417 For *E*, the higher evaporation rates (> 1.8 mm day^{-1}) over the lake area and in

418 the western (southern) from the reference data are well reproduced by the WRF model

419 with slight overestimations (underestimations), except for the low-land region where the

420 observed lower evaporation rates are much overestimated (RME = +20%, Figure 2d-2f).

421 Temporally, the WRF model can reproduce the observed monthly variation in the basin-

422 averaged *E* (*r* = 0.95; *p*-value < 0.01), particularly for the months from August to April

423 (Figure 3b). Moreover, it is found that overestimated *E* during the rainy season (May-

424 July) is coherent with the overestimated *P* during the same period (compare Figure 3b

425 and Figure 3c).

426   For P, the WRF model can reproduce higher (relatively smaller) precipitation

427   rates over the eastern (mid-western) part of the basin, despite observed high

428   precipitation rates (> 5 mm day^{-1}) being much overestimated (ME = +43%, Figure 2g-

429   2i). Figure 3c depicts that the basin-averaged monthly variation in P has a good

430   agreement with that derived from the reference data (r = 0.88; p-value < 0.01),

431   especially the periodic characteristics in P associated with the development of the East

432   Asian summer monsoon. Considerable overestimation of the observed precipitation is

433   found only for the months when maximum rainfall occurs. Such overestimation of P is

434   also found in WRF-based convection-permitting simulations of warm-season P over

435   East China (Yun et al., 2020), although comparatively higher spatial resolution and

436   different physical schemes have been applied. Yun et al. (2020) attributed the WRF

437   overestimated heavy precipitation over mountainous South China to the inappropriate

438   treatment of sub-grid cloud fraction and the lack of representation of aerosol effects. On

439   a short temporal scale, Zhu et al. (2018) focused on evaluating 48-hour WRF forecasts

440   of precipitation over China during the 2013-2014 summer season. They reported that

441   the WRF model overpredicts afternoon convections near Southeast China, which is

442   likely due to deficiencies in the representation of certain physical processes related to

443   precipitation in WRF (e.g., Surcel et al., 2010).

444   Nevertheless, it is argued that our WRF model setup provides state-of-the-art

445   results and can realistically reproduce the climatological characteristics of the East-

446   Asian monsoon-controlled Poyang Lake basin, which encourages us to investigate the

447   alterations of land surface processes and atmospheric water pathways due to global

448   warming with the WRF-age model using this setup.

4.2. Warming-altered land-surface processes

In this section, we investigate the warming-altered land-surface processes for our study region by spatially and temporally comparing the WRF-downscaled future RCP8.5 simulation with the WRF-downscaled historical CTRL simulation for $T2$, E, and P, as shown in Figure 4.

Figure 4a shows the spatial pattern of the simulated 10-year averaged $T2$ in CTRL, displaying that the values of $T2$ in the southern part of the basin are higher than those in the northern part. In comparison to CTRL, the projected 10-year averaged $T2$ in RCP8.5 increases by around +0.5 °C in the southern part of the basin and by around +1.5 °C in the northern part (Figure 4b). Such increases in basin-averaged $T2$ are found throughout the entire year, especially for March, April, and December (> 3 °C), and the highest monthly $T2$ shifts from July in CTRL to August in RCP8.5 (Figure 4c). The spatial pattern of the simulated 10-year averaged E in CTRL shows that the maximum E is found over the lake area (Figure 4d). In comparison to CTRL, the warming enhances the evaporation processes noticeably over the lake area and slightly over the southern part of the basin, whereas the decreased E is pronounced in the areas surrounding the lake (Figure 4e). On the monthly scale, the warming-induced enhancement in E becomes larger from November to August, with a decreased E in May, September, and October (Figure 4f). The largest monthly E shifts from July in CTRL to June in RCP8.5.

The comparison of the simulated P in RCP8.5 with that in CTRL demonstrates that decreases in P are projected for the whole Poyang Lake basin (Figure 4h) and all

471 months except for December when minimal rainfall happens (Figure 4i). Moreover, the

472 monthly variation in the basin-averaged P in RCP8.5 is projected to be lower.

473   Averaged over the basin and over the 10-year time slices, the comparison of

474 RCP8.5 to CTRL shows that global warming leads to increased $T2$ by +1.4 °C, slightly

475 enhanced E by +6%, and noticeably decreased P by -38% for the Poyang Lake basin.

476 Such warmer and drier changes for the Poyang Lake basin have been reported in

477 studies about assessment of regional climate change by evaluating products of multiple

478 global climate models (Lu et al., 2021; Zhang et al., 2022) and multiple regional climate

479 models (Gu et al., 2018). For example, Gu et al. (2018) compared the five RCMs

480 downscaled regional climate over China during 2030-2049 under RCP4.5 to those

481 during the reference historical period 1980-1999. They found that, under RCP4.5, the

482 WRF-projected future changes in temperature and precipitation over Southern China

483 including our study region is +0.5 °C and -15%, which agrees with the sign of changes

484 found in this study. Recent research activities about the assessment of climate change

485 over China under the Coupled Models Intercomparison Project Phase 6 (CMIP6)

486 multiple scenarios confirm that the future climate for the Poyang Lake basin will

487 continuously warm up and become drier in the future (Tian et al., 2021; You et al., 2021;

488 Zhang et al., 2022). As for land evaporation, Lu et al. (2021) evaluated and assessed 16

489 CMIP6 model simulations under three scenarios for China. They found that the land

490 evaporation over the humid region including the Poyang Lake basin during the

491 projection period 2020-2099 shows significant positive trends in comparison to that

492 during the baseline period 1995-2014, which is in line with our finding of the enhanced

493 land evaporation for the Poyang Lake basin under RCP8.5.

494 **4.3. Warming-altered atmospheric water pathways**

495   To quantitively understand the warming-altered regional atmospheric cycle, the

496 analysis of the atmospheric water pathways with the age-weighted regional water

497 tagging approach (Equation 6) is performed. The RCP8.5 and CTRL WRF-age derived

498 quantities of column-integrated tagged water vapor $W_{qv,tag}$, column-integrated tagged

499 condensed atmospheric moisture $W_{qd,tag}$, and tagged precipitation P_{tag}, that are

500 originating from the evaporated water from the Poyang Lake basin, in RCP8.5 are

501 compared spatially and temporally, as shown in Figure 5.

502   Figure 5a shows the spatial pattern of the 10-year averaged column-integrated

503 tagged water vapor $W_{qv,tag}$ over the Poyang Lake basin in CTRL, displaying that larger

504 amounts of the evaporated water (> 0.7 mm) exist over the southeastern part of the

505 basin. In comparison to CTRL, the atmosphere over the Poyang Lake basin in RCP8.5

506 holds more tagged water vapor $W_{qv,tag}$ (Figure 5b), in accordance with the increased $T2$

507 (Figures 4a-4c) and the warming enhanced E (Figures 4d-4f). On the monthly scale, the

508 increases in $W_{qv,tag}$ in RCP8.5 are larger during the warmer and rainy months (March-

509 August) and become negligible during October-December (Figure 5c).

510   The spatial pattern of the 10-year averaged column-integrated tagged condensed

511 atmospheric moisture $W_{qd,tag}$ shown in Figure 5d provides information about clouds and

512 precipitation formation. In comparison to CTRL, warming in RCP8.5 leads to more

513 $W_{qd,tag}$ over the northern part of the basin (Figure 5e), and during the rainy period from

514 April to August (Figure 5f). On the contrary, warming in RCP8.5 leads to less $W_{qd,tag}$ in

515 the atmosphere from September to January (Figure 5f).

516   The comparison of the 10-year averaged tagged precipitation P_{tag} shows that

517   warming in RCP8.5 results in decreased P_{tag} over the basin (Figure 5h). Such

518   decreased P_{tag} in RCP8.5 is projected in nearly every month of the investigated years

519   (Figure 5i).

520   Averaged over the basin and over the 10-year time slices, the atmosphere over

521   the Poyang Lake basin in RCP8.5 will hold more tagged water vapor $W_{qv,tag}$ by +66%,

522   form more tagged clouds $W_{qd,tag}$ by 41%, but generate less tagged precipitation by -83%

523   in comparison to CTRL.

524   **4.4. Warming-altered land-atmosphere interactions**

525   The impact of global warming on the land-atmosphere interactions is quantitively

526   assessed by spatially and temporally comparing the multiple-year averaged contribution

527   ratios $\rho_{qv,tag}$, $\rho_{qd,tag}$, and $\rho_{P,tag}$ (Equation 8) in RCP8.5 with ones in CTRL, as shown in

528   Figure 6.

529   Figure 6a depicts the spatial pattern of the 10-year averaged contribution ratio

530    $\rho_{qv,tag}$ for the column-integrated tagged water vapor $W_{qv,tag}$ in CTRL, revealing that the

531   evaporated water from the Poyang Lake basin has higher contribution (> 3%) to the

532   total water vapor over the western part of the basin and relatively lower contribution (<

533   1%) over the eastern part. In comparison to CTRL, the contribution ratio $\rho_{qv,tag}$ in

534   RCP8.5 is increased by around +3% over the middle-western part of the basin and has

535   no changes over the eastern border of the basin (Figure 6b). Temporally, warming leads

536   to higher increases (+2%) in the contribution ratio $\rho_{qv,tag}$ from February to June, and

537   such increases become less from July to November (Figure 6c)

538   The spatial pattern of $\rho_{qd,tag}$ in Figure 6d shows that in CTRL the contribution

539   ratio of the tagged condensed atmospheric moisture $W_{qd,tag}$ to the total condensed

540   moisture W_{qd} reaches the highest values (> 3%) over the southwestern part of the

541   basin. In comparison to CTRL (Figure 6e), warming leads to increased contribution

542   ratios $\rho_{qd,tag}$ with the highest increases over the area of the lake (+3%). Temporally, the

543   contribution ratios $\rho_{qd,tag}$ in RCP8.5 are higher than those in CTRL from February to

544   August but lower from September to January (Figure 6f).

545   Figure 6g reveals that the contribution $\rho_{P,tag}$ of the evaporated water to the

546   precipitation over the same basin in CTRL is around 3.5%, with the highest values (5%)

547   over the eastern part adjacent to the lake area and the southern part where the

548   mountainous regions are. In comparison to CTRL, the contribution ratio $\rho_{P,tag}$ in

549   RCP8.5 decreases over the entire basin (Figure 6h), and throughout the whole year

550   (Figure 6i).

551   Averaged over the basin and over the 10-year time slices, the comparison of

552   RCP8.5 to CTRL suggests that global warming will slightly strengthen the land-

553   atmosphere interactions with respect to water vapor (by +2%) and clouds (by +1%), but

554   will weaken the interactions with respect to precipitation (by -1%).

4.5. Warming-altered speed of the atmospheric water cycle

556   The impact of global warming on the speed of the atmospheric water cycle is

557   quantitively assessed by spatially and temporally comparing the multiple-year averaged

558   atmospheric residence time $\tau_{qv,tag}$, $\tau_{qd,tag}$ (Equation 9) and atmospheric transit time

559    $T_{P,tag}$ (Equation 10) in RCP8.5 with these in CTRL, as shown in Figure 7.

560   Figure 7a shows the spatial pattern of the 10-year averaged atmospheric

561   residence times $\tau_{qv,tag}$ in CTRL, displaying that the evaporated water from the Poyang

562   Lake basin stays short (~15 hours) in the atmosphere particularly over the lowland lake

563   and its southwestern surroundings (see Figure 1b), and stays longer (> 22 hours) over

564   relatively high-elevation mountainous region (see Figure 1b). In comparison to CTRL,

565   the atmospheric residence times $\tau_{qv,tag}$ in RCP8.5 are projected to be shorter (Figure

566   7b). The monthly variation in $\tau_{qv,tag}$ in RCP8.5 becomes larger than that in CTRL

567   (Figure 7c), and the shortest atmospheric residence times $\tau_{qv,tag}$ are found in October-

568   December in RCP8.5 (around 10 hours), but in July in CTRL (around 15 hours).

569   The spatial pattern of the 10-year averaged atmospheric residence times $\tau_{qd,tag}$

570   in CTRL (Figure 7d) shows that in general the larger amount of the column-integrated

571   tagged condensed moisture $W_{qd,tag}$ (> 0.003 mm shown in Figure 5d) has shorter

572   atmospheric residence time (< 24 hours), whereas the smaller amount of $W_{qd,tag}$ (<

573   0.002 mm in Figure 5d) has longer atmospheric residence time (> 28 hours). In

574   comparison to CTRL, warming in RCP8.5 leads to shorter atmospheric residence times

575    $\tau_{qd,tag}$ over the entire basin and also changed spatial distributions of $\tau_{qd,tag}$, i.e., shorter

576   (longer) $\tau_{qd,tag}$ over the eastern (western) part of the basin (Figure 7e). Temporally,

577   warming in RCP8.5 increases the monthly variation in $\tau_{qd,tag}$, and the atmospheric

578   residence times $\tau_{qd,tag}$ in RCP8.5 becomes shorter (longer) during the period

579   September-April (May-August) than these in CTRL (Figure 7f).

580   Regarding the spatial patterns of $T_{P,tag}$, the tagged precipitation in CTRL has

581   shorter (longer) atmospheric transit times over the southern (northwestern) part of the

582 basin (Figure 7g). In comparison to CTRL, the similar pattern of $T_{P,tag}$ in RCP8.5 is

583 found, but with an increased magnitude of $T_{P,tag}$ and increased corresponding spatial

584 variation (Figure 7h). Temporally, warming in RCP8.5 increases the atmospheric transit

585 times $T_{P,tag}$ and decreases the temporal variation in $T_{P,tag}$ than these in CTRL (Figure

586 7i). The periodic characteristic of $T_{P,tag}$ in CTRL, that is lower values of $T_{P,tag}$ from early

587 summer to early autumn and higher values of $T_{P,tag}$ from late autumn to early spring,

588 still exist in RCP8.5, except for two additional months (October and November) with

589 lower values of $T_{P,tag}$ in RCP8.5.

590   Averaged over the basin and over the 10-year time slices, the comparison of

591 RCP8.5 to CTRL suggests that global warming will shorten the residence times of the

592 tagged water vapor by 8 hours and the tagged condensed moisture by 12 hours in the

593 atmosphere, but will prolong the transit times of the tagged precipitation by 4 hours over

594 the land surface, for the Poyang Lake basin.

595   To understand the contrasting results of the acceleration of the tagged clouds in

596 the atmosphere (Figure 7d-f) and the deceleration of the tagged precipitation over the

597 land surface (Figure 7g-i), we further derive the atmosphere transit time of the column-

598 integrated tagged condensed atmospheric moisture due to fallout $T_{qd\_fallout,tag}$ (see

599 Equations 6 and 7), as shown in Figure 8. It is worth noting that, as the WSM5

600 microphysics scheme is used in this study, the tagged condensed atmospheric moisture

601 (Figure 5d) consists of the non-precipitating tagged liquid water substance (cloud

602 droplets), non-precipitating solid water substance (cloud ice particles), *precipitating*

603 liquid water substance (rain droplets), and *precipitating* solid water substance

604 (snowflakes and other solid forms). The tagged condensed atmospheric moisture due to

605　fallout provides information about the precipitating moisture components only. It is found

606　that the spatial pattern of the atmospheric transit time $T_{qd\_fallout,tag}$ in CTRL (Figure 8a)

607　is similar to that of the tagged precipitation (Figure 7g). In comparison to CTRL,

608　warming leads to increased $T_{qd\_fallout,tag}$ in the eastern part of the basin and decreased

609　in the western part (Figure 8b). Temporally, warming results in increased $T_{qd\_fallout,tag}$

610　from March to September and decreased $T_{qd\_fallout,tag}$ from October to January (Figure

611　8c), which is consistent with the warming-included changes in $T_{P,tag}$ (Figure 7i). Such

612　consistent temporal variations of $T_{qd\_fallout,tag}$ and $T_{P,tag}$ reveal that global warming will

613　modify the precipitating regime over the Poyang Lake basin: Under global warming, the

614　fallout of precipitating moisture components in the atmosphere will take more time,

615　thereby resulting in increased $T_{P,tag}$ over the land surface.

6. Summary and Conclusions

617　　　This study presents the newly developed WRF-age model, that is the Weather

618　Research and Forecasting WRF model of Skamarock et al. (2008) with the

619　implementations of the age-weighed regional water tagging approach from Wei et al.

620　(2016) and the online moisture budget analysis of Arnault et al. (2016) extended for the

621　aged-weighted water. The new model allows us to follow the atmospheric water

622　pathways, to derive atmospheric water residence times, i.e., a measure of the speed of

623　the atmospheric water cycle, and to provide a prognostic equation of the atmospheric

624　water residence times. The WRF-age model has been used to dynamically downscale

625　the reanalysis of ERA-Interim and the MPI-ESM RCP8.5 scenario simulation for the

626　Poyang Lake basin, for two 10-year time slices of past (1980-1989) and future (2040-

627　2049) climate. In these WRF-age simulations, the Poyang Lake basin is chosen as the

628　source of tagged moisture for the age tracing algorithm. The contribution ratio, the

629　residence time of atmospheric water states of matter, and the corresponding

630　atmospheric transit time have been employed to quantitatively assess the regionally

631　accelerated/decelerated atmospheric hydrological cycle under global warming.

632　　　　In comparison to the historical WRF-age simulation, the 2-meter air temperature

633　rises on average by +1.4 °C, evaporation increases by +6%, and precipitation

634　decreases by -38% in the future under RCP8.5. In this context, global warming will

635　shorten the residence times of the tagged water vapor by 8 hours and the tagged

636　condensed moisture by 12 hours in the atmosphere, but will prolong the transit times of

637　the tagged precipitation by 4 hours over the land surface that is in agreement with the

638　reduced land precipitation amounts. Such prolonged atmospheric transit time of land

639　precipitation under global warming is partly attributed to a slower fallout of precipitating

640　moisture components in the atmosphere under global warming. We also found that

641　global warming will lead to slightly increased contributions of the evaporation to the

642　water vapor and the condensed atmospheric moisture over the Poyang Lake basin, but

643　slightly decreased contributions of the evaporation to the precipitation. These distinct,

644　warming-induced changes in the contribution ratios suggest that global warming will

645　alter the local land-atmosphere interactions over the Poyang Lake basin.

646　　　　This first study with WRF-age demonstrates the potential of this model for

647　deriving the residence times of atmospheric water states of matter, with the

648　considerations of three-dimensional physical and thermodynamical processes in the

649　atmosphere and the interactions of land-atmosphere. Moreover, our warming-induced

650 acceleration findings demonstrate that global warming increases the complexity of the

651 regional atmospheric hydrological cycle, especially the associated changes in the speed

652 of atmospheric water states of matter. Overall, it is concluded that our modeling study

653 confirms the acceleration of the regional atmospheric water cycle under global warming,

654 except for the precipitation-related processes. Our findings enhance the understanding

655 of the warming-induced acceleration/deceleration of the atmospheric hydrological cycle

656 at regional scales.

657 Despite the above-mentioned advanced features of our newly developed WRF-

658 age model, one potential limitation of our RCM-based age-weighted regional water

659 tagging approach is that the model-derived results of tracked evaporated water and

660 respective atmospheric residence times depend on how realistically an RCM can

661 simulate all the relevant processes of terrestrial hydrology, vegetation, and atmosphere

662 (Gimeno et al., 2012). Direct validation of our model-derived results would be possible

663 by tracking the water isotopologues as done in, e.g., Arnault, Jung, et al. (2021) and

664 Arnault et al. (2022).

665 **Acknowledgments**

679   **References**

680   Allen, M. R., & Ingram, W. J. (2002). Constraints on future changes in climate and the

681   hydrologic cycle. *Nature*, *419*(6903), 224–32. https://doi.org/10.1038/nature01092

682   Armstrong McKay, D. I., Staal, A., Abrams, J. F., Winkelmann, R., Sakschewski, B., Loriani, S.,

683   et al. (2022). Exceeding 1.5°C global warming could trigger multiple climate tipping

684   points. *Science*, *377*(6611), eabn7950. https://doi.org/10.1126/science.abn7950

685   Arnault, Joel, Knoche, R., Wei, J., & Kunstmann, H. (2016a). Evaporation tagging and

686   atmospheric water budget analysis with WRF: A regional precipitation recycling study

687   for West Africa. *Water Resources Research*, *52*(3), 1544–1567.

688   https://doi.org/10.1002/2015WR017704

689   Arnault, Joel, Knoche, R., Wei, J., & Kunstmann, H. (2016b). Evaporation tagging and

690   atmospheric water budget analysis with WRF: A regional precipitation recycling study

691   for West Africa. *Water Resources Research*, *52*(3), 1544–1567.

692   https://doi.org/10.1002/2015WR017704

693   Arnault, Joël, Wei, J., Rummler, T., Fersch, B., Zhang, Z., Jung, G., et al. (2019). A Joint Soil-

694   Vegetation-Atmospheric Water Tagging Procedure With WRF-Hydro: Implementation

695   and Application to the Case of Precipitation Partitioning in the Upper Danube River

696   Basin. *Water Resources Research*, *55*(7), 6217–6243.

697   https://doi.org/10.1029/2019WR024780

698 Arnault, Joël, Jung, G., Haese, B., Fersch, B., Rummler, T., Wei, J., et al. (2021). A Joint Soil-

699   Vegetation-Atmospheric Modeling Procedure of Water Isotopologues: Implementation

700   and Application to Different Climate Zones With WRF-Hydro-Iso. *Journal of Advances*

701   *in Modeling Earth Systems*, *13*(10), e2021MS002562.

702   https://doi.org/10.1029/2021MS002562

703 Arnault, Joël, Fersch, B., Rummler, T., Zhang, Z., Quenum, G. M., Wei, J., et al. (2021). Lateral

704   terrestrial water flow contribution to summer precipitation at continental scale – A

705   comparison between Europe and West Africa with WRF-Hydro-tag ensembles.

706   *Hydrological Processes*, *35*(5). https://doi.org/10.1002/hyp.14183

707 Arnault, Joël, Niezgoda, K., Jung, G., Hahn, A., Zabel, M., Schefuß, E., & Kunstmann, H.

708   (2022). Disentangling the Contribution of Moisture Source Change to Isotopic Proxy

709   Signatures: Deuterium Tracing with WRF-Hydro-Iso-Tag and Application to Southern

710   African Holocene Sediment Archives. *Journal of Climate*, *35*(22), 3855–3879.

711   https://doi.org/10.1175/JCLI-D-22-0041.1

712 Benedict, I., van Heerwaarden, C. C., van der Linden, E. C., Weerts, A. H., & Hazeleger, W.

713   (2021). Anomalous moisture sources of the Rhine basin during the extremely dry

714   summers of 2003 and 2018. *Weather and Climate Extremes*, *31*, 100302.

715   https://doi.org/10.1016/j.wace.2020.100302

716 Betts, A. K. (1986). A new convective adjustment scheme. Part I: Observational and theoretical

717   basis. *Quarterly Journal of the Royal Meteorological Society*.

718   https://doi.org/10.1002/qj.49711247307

719   Betts, A. K., & Miller, M. J. (1986). A new convective adjustment scheme. Part II: Single

720   column tests using GATE wave, BOMEX, ATEX and arctic air-mass data sets. *Quarterly*

721   *Journal of the Royal Meteorological Society*. https://doi.org/10.1002/qj.49711247308

722   Betts, Alan K., Ball, J. H., Beljaars, A. C. M., Miller, M. J., & Viterbo, P. A. (1996). The land

723   surface-atmosphere interaction: A review based on observational and global modeling

724   perspectives. *Journal of Geophysical Research*, *101*(D3), 7209.

725   https://doi.org/10.1029/95JD02135

726   Blöschl, G., Bierkens, M. F. P., Chambel, A., Cudennec, C., Destouni, G., Fiori, A., et al. (2019).

727   Twenty-three unsolved problems in hydrology (UPH) – a community perspective.

728   *Hydrological Sciences Journal*, *64*(10), 1141–1158.

729   https://doi.org/10.1080/02626667.2019.1620507

730   Bosilovich, M. G. (2002). On the vertical distribution of local and remote sources of water for

731   precipitation. *Meteorology and Atmospheric Physics*, *80*(1–4), 31–41.

732   https://doi.org/10.1007/s007030200012

733   Bosilovich, Michael G., & Schubert, S. D. (2001). Precipitation Recycling over the Central

734   United States Diagnosed from the GEOS-1 Data Assimilation System. *Journal of*

735   *Hydrometeorology*, *2*(1), 26–35. https://doi.org/10.1175/1525-

736   7541(2001)002<0026:PROTCU>2.0.CO;2

737   Bosilovich, Michael G, & Schubert, S. D. (2002). Water Vapor Tracers as Diagnostics of the

738   Regional Hydrologic Cycle. *Journal of Hydrometeorology*, *3*(2), 149–165.

739   https://doi.org/10.1175/1525-7541(2002)003<0149:WVTADO>2.0.CO;2

740   Bosilovich, Michael G., Schubert, S. D., & Walker, G. K. (2005). Global Changes of the Water

741   Cycle Intensity. *Journal of Climate*, *18*(10), 1591–1608.

742   https://doi.org/10.1175/JCLI3357.1

743   Braun, S. A. (2006). High-Resolution Simulation of Hurricane Bonnie (1998). Part II: Water

744   Budget. *Journal of the Atmospheric Sciences*, *63*(1), 43–64.

745   https://doi.org/10.1175/JAS3609.1

746   Chen, F., & Dudhia, J. (2001). Coupling an Advanced Land Surface–Hydrology Model with the

747   Penn State–NCAR MM5 Modeling System. Part I: Model Implementation and

748   Sensitivity. *Monthly Weather Review*, *129*(4), 569–585. https://doi.org/10.1175/1520-

749   0493(2001)129<0587:CAALSH>2.0.CO;2

750   Dee, D. P., Uppala, S. M., Simmons, A. J., Berrisford, P., Poli, P., Kobayashi, S., et al. (2011).

751   The ERA-Interim reanalysis: configuration and performance of the data assimilation

752   system. *Quarterly Journal of the Royal Meteorological Society*, *137*(656), 553–597.

753   https://doi.org/10.1002/qj.828

754   Ding, Y., & Chan, J. C. L. (2005). The East Asian summer monsoon: an overview. *Meteorology*

755   *and Atmospheric Physics*, *89*(1–4), 117–142. https://doi.org/10.1007/s00703-005-0125-z

756   Dirmeyer, P. A., & Brubaker, K. L. (2007). Characterization of the Global Hydrologic Cycle

757   from a Back-Trajectory Analysis of Atmospheric Water Vapor. *Journal of*

758   *Hydrometeorology*, *8*(1), 20–37. https://doi.org/10.1175/JHM557.1

759   Dominguez, F., Miguez-Macho, G., & Hu, H. (2016). WRF with Water Vapor Tracers: A Study

760   of Moisture Sources for the North American Monsoon. *Journal of Hydrometeorology*,

761   *17*(7), 1915–1927. https://doi.org/10.1175/JHM-D-15-0221.1

762   Dudhia, J. (1989). Numerical Study of Convection Observed during the Winter Monsoon

763   Experiment Using a Mesoscale Two-Dimensional Model. *Journal of the Atmospheric*

764   *Sciences*, *46*(20), 3077–3107. https://doi.org/10.1175/1520-

765   0469(1989)046<3077:NSOCOD>2.0.CO;2

766   Dudhia, J. (1993). A Nonhydrostatic Version of the Penn State–NCAR Mesoscale Model:

767   Validation Tests and Simulation of an Atlantic Cyclone and Cold Front. *Monthly*

768   *Weather Review*, *121*(5), 1493–1513. https://doi.org/10.1175/1520-

769   0493(1993)121<1493:ANVOTP>2.0.CO;2

770   van der Ent, R. J., Tuinenburg, O. A., Knoche, H.-R., Kunstmann, H., & Savenije, H. H. G.

771   (2013). Should we use a simple or complex model for moisture recycling and

772   atmospheric moisture tracking? *Hydrology and Earth System Sciences*, *17*(12), 4869–

773   4884. https://doi.org/10.5194/hess-17-4869-2013

774   van der Ent, R. J., Wang-Erlandsson, L., Keys, P. W., & Savenije, H. H. G. (2014). Contrasting

775   roles of interception and transpiration in the hydrological cycle – Part 2: Moisture

776   recycling. *Earth System Dynamics*, *5*(2), 471–489. https://doi.org/10.5194/esd-5-471-

777   2014

778   van der Ent, Rudi J., Savenije, H. H. G., Schaefli, B., & Steele-Dunne, S. C. (2010). Origin and

779   fate of atmospheric moisture over continents. *Water Resources Research*, *46*(9), n/a-n/a.

780   https://doi.org/10.1029/2010WR009127

781   van der Ent, Ruud J., & Tuinenburg, O. A. (2017). The residence time of water in the atmosphere

782   revisited. *Hydrology and Earth System Sciences*, *21*(2), 779–790.

783   https://doi.org/10.5194/hess-21-779-2017

784   Feng, L., Hu, C., Chen, X., Li, R., Tian, L., & Murch, B. (2011). MODIS observations of the

785   bottom topography and its inter-annual variability of Poyang Lake. *Remote Sensing of*

786   *Environment*, *115*(10), 2729–2741. https://doi.org/10.1016/j.rse.2011.06.013

787   Fersch, B., & Kunstmann, H. (2014). Atmospheric and terrestrial water budgets: sensitivity and

788   performance of configurations and global driving data for long term continental scale

789   WRF simulations. *Climate Dynamics*, *42*(9–10), 2367–2396.

790   https://doi.org/10.1007/s00382-013-1915-5

791   Ficklin, D. L., Abatzoglou, J. T., & Novick, K. A. (2019). A New Perspective on Terrestrial

792   Hydrologic Intensity That Incorporates Atmospheric Water Demand. *Geophysical*

793   *Research Letters*, *46*(14), 8114–8124. https://doi.org/10.1029/2019GL084015

794   Ficklin, D. L., Null, S. E., Abatzoglou, J. T., Novick, K. A., & Myers, D. T. (2022).

795   Hydrological Intensification Will Increase the Complexity of Water Resource

796   Management. *Earth's Future*, *10*(3), e2021EF002487.

797   https://doi.org/10.1029/2021EF002487

798   Fita, L., Polcher, J., Giannaros, T. M., Lorenz, T., Milovac, J., Sofiadis, G., et al. (2019).

799   CORDEX-WRF v1.3: development of a module for the Weather Research and

800   Forecasting (WRF) model to support the CORDEX community. *Geoscientific Model*

801   *Development*, *12*(3), 1029–1066. https://doi.org/10.5194/gmd-12-1029-2019

802   Gao, L., Wei, J., Lei, X., Ma, M., Wang, L., Guan, X., & Lin, H. (2022). Simulation of an

803   Extreme Precipitation Event Using Ensemble-Based WRF Model in the Southeastern

804   Coastal Region of China. *Atmosphere*, *13*(2), 194.

805   https://doi.org/10.3390/atmos13020194

806   Gimeno, L., Stohl, A., Trigo, R. M., Dominguez, F., Yoshimura, K., Yu, L., et al. (2012).

807   Oceanic and terrestrial sources of continental precipitation. *Reviews of Geophysics*, *50*(4),

808   RG4003. https://doi.org/10.1029/2012RG000389

809   Gimeno, L., Eiras-Barca, J., Durán-Quesada, A. M., Dominguez, F., van der Ent, R., Sodemann,

810   H., et al. (2021). The residence time of water vapour in the atmosphere. *Nature Reviews*

811   *Earth & Environment*, *2*(8), 558–569. https://doi.org/10.1038/s43017-021-00181-9

812   Giorgetta, M. A., Jungclaus, J., Reick, C. H., Legutke, S., Bader, J., Böttinger, M., et al. (2013).

813   Climate and carbon cycle changes from 1850 to 2100 in MPI-ESM simulations for the

814   Coupled Model Intercomparison Project phase 5. *Journal of Advances in Modeling Earth*

815   *Systems*, *5*(3), 572–597. https://doi.org/10.1002/jame.20038

816   Giorgi, F., Im, E.-S., Coppola, E., Diffenbaugh, N. S., Gao, X. J., Mariotti, L., & Shi, Y. (2011).

817   Higher Hydroclimatic Intensity with Global Warming. *Journal of Climate*, *24*(20), 5309–

818   5324. https://doi.org/10.1175/2011JCLI3979.1

819   Giorgi, F., Coppola, E., & Raffaele, F. (2014). A consistent picture of the hydroclimatic response

820   to global warming from multiple indices: Models and observations. *Journal of*

821   *Geophysical Research: Atmospheres*, *119*(20), 11,695-11,708.

822   https://doi.org/10.1002/2014JD022238

823   Goessling, H. F., & Reick, C. H. (2013). On the "well-mixed" assumption and numerical 2-D

824   tracing of atmospheric moisture. *Atmospheric Chemistry and Physics*, *13*(11), 5567–

825   5585. https://doi.org/10.5194/acp-13-5567-2013

826   Grell, A. G., Dudhia, J., & Stauffer, R. D. (1994). *A description of the fifth-generation Penn*

827   *State/NCAR Mesoscale Model (MM5)*. https://doi.org/10.5065/D60Z716B

828   Gu, H., Yu, Z., Wang, J., Wang, G., Yang, T., Ju, Q., et al. (2015). Assessing CMIP5 general

829   circulation model simulations of precipitation and temperature over China. *International*

830   *Journal of Climatology*, *35*(9), 2431–2440. https://doi.org/10.1002/joc.4152

831   Gu, H., Yu, Z., Yang, C., Ju, Q., Yang, T., & Zhang, D. (2018). High-resolution ensemble

832   projections and uncertainty assessment of regional climate change over China in

833   CORDEX East Asia. *Hydrology and Earth System Sciences*, *22*(5), 3087–3103.

834   https://doi.org/10.5194/hess-22-3087-2018

835   Gu, L., Yin, J., Slater, L. J., Chen, J., Do, H. X., Wang, H.-M., et al. (2023). Intensification of

836   Global Hydrological Droughts Under Anthropogenic Climate Warming. *Water Resources*

837   *Research*, *59*(1), e2022WR032997. https://doi.org/10.1029/2022WR032997

838   Hao, Z. (2022). Compound events and associated impacts in China. *IScience*, *25*(8), 104689.

839   https://doi.org/10.1016/j.isci.2022.104689

840   Held, I. M., & Soden, B. J. (2006). Robust Responses of the Hydrological Cycle to Global

841   Warming. *Journal of Climate*, *19*(21), 5686–5699. https://doi.org/10.1175/JCLI3990.1

842   Hong, S.-Y., Dudhia, J., & Chen, S.-H. (2004). A Revised Approach to Ice Microphysical

843   Processes for the Bulk Parameterization of Clouds and Precipitation. *Monthly Weather*

844   *Review*, *132*(1), 103–120. https://doi.org/10.1175/1520-

845   0493(2004)132<0103:ARATIM>2.0.CO;2

846   Hong, S.-Y., Noh, Y., Dudhia, J., Hong, S.-Y., Noh, Y., & Dudhia, J. (2006). A New Vertical

847   Diffusion Package with an Explicit Treatment of Entrainment Processes. *Monthly*

848   *Weather Review*, *134*(9), 2318–2341. https://doi.org/10.1175/MWR3199.1

849   Hu, X., Hall, J. W., Shi, P., & Lim, W. H. (2016). The spatial exposure of the Chinese

850   infrastructure system to flooding and drought hazards. *Natural Hazards*, *80*(2), 1083–

851   1118. https://doi.org/10.1007/s11069-015-2012-3

852   Huntington, T. G. (2006). Evidence for intensification of the global water cycle: Review and

853   synthesis. *Journal of Hydrology*, *319*(1–4), 83–95.

854   https://doi.org/10.1016/j.jhydrol.2005.07.003

855   Huntington, T. G., Weiskel, P. K., Wolock, D. M., & McCabe, G. J. (2018). A new indicator

856   framework for quantifying the intensity of the terrestrial water cycle. *Journal of*

857   *Hydrology*, *559*, 361–372. https://doi.org/10.1016/j.jhydrol.2018.02.048

858   Hurk, B. van den, Best, M., Dirmeyer, P., Pitman, A., Polcher, J., & Santanello, J. (2011).

859   Acceleration of Land Surface Model Development over a Decade of Glass. *Bulletin of the*

860   *American Meteorological Society*, *92*(12), 1593–1600. https://doi.org/10.1175/BAMS-D-

861   11-00007.1

862   Janjić, Z. I. (2002). Comments on "Development and Evaluation of a Convection Scheme for

863   Use in Climate Models." *Journal of the Atmospheric Sciences*.

864   https://doi.org/10.1175/1520-0469(2000)057<3686:codaeo>2.0.co;2

865   Jiménez, P. A., Dudhia, J., González-Rouco, J. F., Navarro, J., Montávez, J. P., & García-

866   Bustamante, E. (2012). A Revised Scheme for the WRF Surface Layer Formulation.

867   *Monthly Weather Review*, *140*(3), 898–918. https://doi.org/10.1175/mwr-d-11-00056.1

868   Knoche, H. R., & Kunstmann, H. (2013). Tracking atmospheric water pathways by direct

869   evaporation tagging: A case study for West Africa. *Journal of Geophysical Research:*

870   *Atmospheres*, *118*(22), 12,345-12,358. https://doi.org/10.1002/2013JD019976

871 Läderach, A., & Sodemann, H. (2016). A revised picture of the atmospheric moisture residence

872   time. *Geophysical Research Letters*. https://doi.org/10.1002/2015GL067449

873 Langhans, W., Schmidli, J., Schär, C., Langhans, W., Schmidli, J., & Schär, C. (2012). Bulk

874   Convergence of Cloud-Resolving Simulations of Moist Convection over Complex

875   Terrain. *Journal of the Atmospheric Sciences*, *69*(7), 2207–2228.

876   https://doi.org/10.1175/JAS-D-11-0252.1

877 Langhans, W., Fuhrer, O., & Schmidli, J. (2012). Description and application of a budget

878   diagnosis tool in COSMO. In *COSMO Newsletter* (p. No. 12, 43-51).

879 Lenton, T. M., Held, H., Kriegler, E., Hall, J. W., Lucht, W., Rahmstorf, S., & Schellnhuber, H.

880   J. (2008). Tipping elements in the Earth's climate system. *Proceedings of the National*

881   *Academy of Sciences*, *105*(6), 1786–1793. https://doi.org/10.1073/pnas.0705414105

882 Li, J., Wu, Z., Jiang, Z., & He, J. (2010). Can Global Warming Strengthen the East Asian

883   Summer Monsoon? *Journal of Climate*, *23*(24), 6696–6705.

884   https://doi.org/10.1175/2010JCLI3434.1

885 Li, Xianghu, & Zhang, Q. (2011). Estimating the Potential Evapotranspiration of Poyang Lake

886   Basin Using Remote Sense Data and Shuttleworth-Wallace Model. *Procedia*

887   *Environmental Sciences*, *10*, 1575–1582. https://doi.org/10.1016/j.proenv.2011.09.250

888 Li, Xin, Fang, G., Wei, J., Arnault, J., Laux, P., Wen, X., & Kunstmann, H. (2023). Evaluation

889   and projection of precipitation and temperature in a coastal climatic transitional zone in

890   China based on CMIP6 GCMs. *Climate Dynamics*. https://doi.org/10.1007/s00382-023-

891   06781-z

892   Liu, L., Gao, J., & Wu, S. (2022). Warming of 0.5 °C may cause double the economic

893   loss and increase the population affected by floods in China. *Natural Hazards and Earth*

894   *System Sciences*, *22*(5), 1577–1590. https://doi.org/10.5194/nhess-22-1577-2022

895   Lu, J., Wang, G., Li, S., Feng, A., Zhan, M., Jiang, T., et al. (2021). Projected Land Evaporation

896   and Its Response to Vegetation Greening Over China Under Multiple Scenarios in the

897   CMIP6 Models. *Journal of Geophysical Research: Biogeosciences*, *126*(9),

898   e2021JG006327. https://doi.org/10.1029/2021JG006327

899   Martens, B., Miralles, D. G., Lievens, H., van der Schalie, R., de Jeu, R. A. M., Fernández-

900   Prieto, D., et al. (2017). GLEAM v3: satellite-based land evaporation and root-zone soil

901   moisture. *Geoscientific Model Development*, *10*(5), 1903–1925.

902   https://doi.org/10.5194/gmd-10-1903-2017

903   Milovac, J., Warrach-Sagi, K., Behrendt, A., Späth, F., Ingwersen, J., & Wulfmeyer, V. (2016).

904   Investigation of PBL schemes combining the WRF model simulations with scanning

905   water vapor differential absorption lidar measurements. *Journal of Geophysical*

906   *Research: Atmospheres*, *121*(2), 624–649. https://doi.org/10.1002/2015JD023927

907   Mlawer, E. J., Taubman, S. J., Brown, P. D., Iacono, M. J., & Clough, S. A. (1997). Radiative

908   transfer for inhomogeneous atmospheres: RRTM, a validated correlated-k model for the

909   longwave. *Journal of Geophysical Research*, *102*(D14), 16663.

910   https://doi.org/10.1029/97JD00237

911   Mohan, T. S., & Rajeevan, M. (2017). Past and future trends of hydroclimatic intensity over the

912   Indian monsoon region. *Journal of Geophysical Research: Atmospheres*, *122*(2), 896–

913   909. https://doi.org/10.1002/2016JD025301

914   Mori, P., Schwitalla, T., Ware, M. B., Warrach-Sagi, K., & Wulfmeyer, V. (2020). Downscaling

915   of seasonal ensemble forecasts to the convection-permitting scale over the Horn of Africa

916   using the WRF model. *International Journal of Climatology*.

917   https://doi.org/10.1002/joc.6809

918   Numaguti, A. (1999). Origin and recycling processes of precipitating water over the Eurasian

919   continent: Experiments using an atmospheric general circulation model. *Journal of*

920   *Geophysical Research*, *104*(D2), 1957. https://doi.org/10.1029/1998JD200026

921   Olmedo, E., Turiel, A., González-Gambau, V., González-Haro, C., García-Espriu, A., Gabarró,

922   C., et al. (2022). Increasing stratification as observed by satellite sea surface salinity

923   measurements. *Scientific Reports*, *12*(1), 6279. https://doi.org/10.1038/s41598-022-

924   10265-1

925   Olschewski, P., Laux, P., Wei, J., Böker, B., Tian, Z., Sun, L., & Kunstmann, H. (2023). An

926   ensemble-based assessment of bias adjustment performance, changes in

927   hydrometeorological predictors and compound extreme events in EAS-CORDEX.

928   *Weather and Climate Extremes*, *39*, 100531. https://doi.org/10.1016/j.wace.2022.100531

929   Santanello, J. A., Dirmeyer, P. A., Ferguson, C. R., Findell, K. L., Tawfik, A. B., Berg, A., et al.

930   (2018). Land-atmosphere interactions the LoCo perspective. *Bulletin of the American*

931   *Meteorological Society*. https://doi.org/10.1175/BAMS-D-17-0001.1

932   Shang, S., Zhu, G., Wei, J., Li, Y., Zhang, K., Li, R., et al. (2021). Associated Atmospheric

933   Mechanisms for the Increased Cold Season Precipitation over the Three-River

934   Headwaters Region from the Late 1980s. *Journal of Climate*, *34*(19), 8033–8046.

935   https://doi.org/10.1175/JCLI-D-21-0077.1

936 Shang, S., Arnault, J., Zhu, G., Chen, H., Wei, J., Zhang, K., et al. (2022). Recent Increase of

937   Spring Precipitation over the Three-River Headwaters Region—Water Budget Analysis

938   Based on Global Reanalysis (ERA5) and ET-Tagging Extended Regional Climate

939   Modeling. *Journal of Climate*, *35*(22), 3599–3617. https://doi.org/10.1175/JCLI-D-21-

940   0829.1

941 Siegmund, J., Bliefernicht, J., Laux, P., & Kunstmann, H. (2015). Toward a seasonal

942   precipitation prediction system for West Africa: Performance of CFSv2 and high-

943   resolution dynamical downscaling. *Journal of Geophysical Research: Atmospheres*,

944   *120*(15), 7316–7339. https://doi.org/10.1002/2014JD022692

945 Singh, H. A., Bitz, C. M., Nusbaumer, J., & Noone, D. C. (2016). A mathematical framework for

946   analysis of water tracers: Part 1: Development of theory and application to the

947   preindustrial mean state. *Journal of Advances in Modeling Earth Systems*, *8*(2), 991–

948   1013. https://doi.org/10.1002/2016MS000649

949 Singh, H. K. A., Bitz, C. M., Donohoe, A., Nusbaumer, J., & Noone, D. C. (2016). A

950   Mathematical Framework for Analysis of Water Tracers. Part II: Understanding Large-

951   Scale Perturbations in the Hydrological Cycle due to CO2 Doubling. *Journal of Climate*,

952   *29*(18), 6765–6782. https://doi.org/10.1175/JCLI-D-16-0293.1

953 Skamarock, W., Klemp, J., Dudhia, J., Gill, D., Barker, D., Wang, W., et al. (2008). A

954   Description of the Advanced Research WRF Version 3. *NCAR Technical Note

955   NCAR/TN-475+STR*. https://doi.org/10.5065/D68S4MVH

956 Sodemann, H., Wernli, H., & Schwierz, C. (2009). Sources of water vapour contributing to the

957   Elbe flood in August 2002-A tagging study in a mesoscale model. *Quarterly Journal of

958   the Royal Meteorological Society*, *135*(638), 205–223. https://doi.org/10.1002/qj.374

959   Stohl, A., & James, P. (2004). A Lagrangian Analysis of the Atmospheric Branch of the Global

960   Water Cycle. Part I: Method Description, Validation, and Demonstration for the August

961   2002 Flooding in Central Europe. *Journal of Hydrometeorology*, *5*(4), 656–678.

962   https://doi.org/10.1175/1525-7541(2004)005<0656:ALAOTA>2.0.CO;2

963   Su, B., Huang, J., Fischer, T., Wang, Y., Kundzewicz, Z. W., Zhai, J., et al. (2018). Drought

964   losses in China might double between the 1.5 °C and 2.0 °C warming. *Proceedings of the*

965   *National Academy of Sciences*, *115*(42), 10600–10605.

966   https://doi.org/10.1073/pnas.1802129115

967   Surcel, M., Berenguer, M., & Zawadzki, I. (2010). The Diurnal Cycle of Precipitation from

968   Continental Radar Mosaics and Numerical Weather Prediction Models. Part I:

969   Methodology and Seasonal Comparison. *Monthly Weather Review*, *138*(8), 3084–3106.

970   https://doi.org/10.1175/2010MWR3125.1

971   Tian, J., Zhang, Z., Ahmed, Z., Zhang, L., Su, B., Tao, H., & Jiang, T. (2021). Projections of

972   precipitation over China based on CMIP6 models. *Stochastic Environmental Research*

973   *and Risk Assessment*, *35*(4), 831–848. https://doi.org/10.1007/s00477-020-01948-0

974   Trenberth, K. E. (1998). Atmospheric Moisture Residence Times and Cycling: Implications for

975   Rainfall Rates and Climate Change. *Climatic Change*, *39*(4), 667–694.

976   https://doi.org/10.1023/A:1005319109110

977   Trenberth, K. E. (1999). Atmospheric Moisture Recycling: Role of Advection and Local

978   Evaporation. *Journal of Climate*, *12*(5), 1368–1381. https://doi.org/10.1175/1520-

979   0442(1999)012<1368:AMRROA>2.0.CO;2

980   Tuinenburg, O. A., & van der Ent, R. J. (2019). Land Surface Processes Create Patterns in

981   Atmospheric Residence Time of Water. *Journal of Geophysical Research: Atmospheres*,

982   *124*(2), 583–600. https://doi.org/10.1029/2018JD028871

983   Vahmani, P., Jones, A. D., & Li, D. (2022). Will Anthropogenic Warming Increase

984   Evapotranspiration? Examining Irrigation Water Demand Implications of Climate

985   Change in California. *Earth's Future*, *10*(1), e2021EF002221.

986   https://doi.org/10.1029/2021EF002221

987   Wagner, S., Fersch, B., Kunstmann, H., Yuan, F., Yang, C., & Yu, Z. (2013).

988   Hydrometeorological modelling for Poyang Lake region, China. *IAHS-AISH Publication*,

989   *359*, 152–157.

990   Wagner, Sven, Berg, P., Schädler, G., & Kunstmann, H. (2013). High resolution regional climate

991   model simulations for Germany: Part II-projected climate changes. *Climate Dynamics*.

992   https://doi.org/10.1007/s00382-012-1510-1

993   Wagner, Sven, Fersch, B., Yuan, F., Yu, Z., & Kunstmann, H. (2016). Fully coupled

994   atmospheric-hydrological modeling at regional and long-term scales: Development,

995   application, and analysis of WRF-HMS. *Water Resources Research*, *52*(4), 3187–3211.

996   https://doi.org/10.1002/2015WR018185

997   Wang, N., Zeng, X.-M., Zheng, Y., Zhu, J., & Jiang, S. (2018). The Atmospheric Moisture

998   Residence Time and Reference Time for Moisture Tracking over China. *Journal of*

999   *Hydrometeorology*, *19*(7), 1131–1147. https://doi.org/10.1175/JHM-D-17-0204.1

1000   Wang-Erlandsson, L., Fetzer, I., Keys, P. W., van der Ent, R. J., Savenije, H. H. G., & Gordon,

1001   L. J. (2018). Remote land use impacts on river flows through atmospheric

1002   teleconnections. *Hydrology and Earth System Sciences*, *22*(8), 4311–4328.

1003   https://doi.org/10.5194/hess-22-4311-2018

1004   Warrach-Sagi, K., Schwitalla, T., Wulfmeyer, V., & Bauer, H.-S. (2013). Evaluation of a climate

1005   simulation in Europe based on the WRF–NOAH model system: precipitation in

1006   Germany. *Climate Dynamics*, *41*(3–4), 755–774. https://doi.org/10.1007/s00382-013-

1007   1727-7

1008   Wei, J., Knoche, H. R., & Kunstmann, H. (2015). Contribution of transpiration and evaporation

1009   to precipitation: An ET-Tagging study for the Poyang Lake region in Southeast China.

1010   *Journal of Geophysical Research: Atmospheres*, *120*(14), 6845–6864.

1011   https://doi.org/10.1002/2014JD022975

1012   Wei, J., Knoche, H. R., & Kunstmann, H. (2016). Atmospheric residence times from

1013   transpiration and evaporation to precipitation: An age-weighted regional evaporation

1014   tagging approach. *Journal of Geophysical Research: Atmospheres*, *121*(12), 6841–6862.

1015   https://doi.org/10.1002/2015JD024650

1016   Wei, J., Dong, N., Fersch, B., Arnault, J., Wagner, S., Laux, P., et al. (2021). Role of reservoir

1017   regulation and groundwater feedback in a simulated ground-soil-vegetation continuum: A

1018   long-term regional scale analysis. *Hydrological Processes*, *35*(8), e14341.

1019   https://doi.org/10.1002/hyp.14341

1020   Winschall, A., Pfahl, S., Sodemann, H., & Wernli, H. (2014). Comparison of Eulerian and

1021   Lagrangian moisture source diagnostics – the flood event in eastern Europe in May 2010.

1022   *Atmospheric Chemistry and Physics*, *14*(13), 6605–6619. https://doi.org/10.5194/acp-14-

1023   6605-2014

1024   Wu, J., & Gao, X. (2013). A gridded daily observation dataset over China region and comparison

1025   with the other datasets. *Chinese Journal of Geophysics*, *56*(4), 1102–1111.

1026   https://doi.org/10.6038/cjg20130406

1027   Wulfmeyer, V., Turner, D. D., Baker, B., Banta, R., Behrendt, A., Bonin, T., et al. (2018). A

1028   New Research Approach for Observing and Characterizing Land-Atmosphere Feedback.

1029   *Bulletin of the American Meteorological Society*, BAMS-D-17-0009.1.

1030   https://doi.org/10.1175/BAMS-D-17-0009.1

1031   Xing, Z., Yu, Z., Wei, J., Zhang, X., Ma, M., Yi, P., et al. (2022). Lagged influence of ENSO

1032   regimes on droughts over the Poyang Lake basin, China. *Atmospheric Research*, *275*,

1033   106218. https://doi.org/10.1016/j.atmosres.2022.106218

1034   Yang, Q., Yu, Z., Wei, J., Yang, C., Gu, H., Xiao, M., et al. (2021). Performance of the WRF

1035   model in simulating intense precipitation events over the Hanjiang River Basin, China –

1036   A multi-physics ensemble approach. *Atmospheric Research*.

1037   https://doi.org/10.1016/j.atmosres.2020.105206

1038   Yates, D. N., Chen, F., & Nagai, H. (2003). Land Surface Heterogeneity in the Cooperative

1039   Atmosphere Surface Exchange Study (CASES-97). Part II: Analysis of Spatial

1040   Heterogeneity and Its Scaling. *Journal of Hydrometeorology*, *4*(2), 219–234.

1041   https://doi.org/10.1175/1525-7541(2003)4<219:LSHITC>2.0.CO;2

1042   Ye, X., Zhang, Q., Bai, L., & Hu, Q. (2011). A modeling study of catchment discharge to

1043   Poyang Lake under future climate in China. *Quaternary International*, *244*(2), 221–229.

1044   https://doi.org/10.1016/j.quaint.2010.07.004

1045   Yoshimura, K., Oki, T., Ohte, N., & Kanae, S. (2004). Colored Moisture Analysis Estimates of

1046   Variations in 1998 Asian Monsoon Water Sources. *Journal of the Meteorological Society*

1047   *of Japan*, *82*(5), 1315–1329. https://doi.org/10.2151/jmsj.2004.1315

1048   You, Q., Cai, Z., Wu, F., Jiang, Z., Pepin, N., & Shen, S. S. P. (2021). Temperature dataset of

1049   CMIP6 models over China: evaluation, trend and uncertainty. *Climate Dynamics*, *57*(1),

1050   17–35. https://doi.org/10.1007/s00382-021-05691-2

1051   Yu, L., Josey, S. A., Bingham, F. M., & Lee, T. (2020). Intensification of the global water cycle

1052   and evidence from ocean salinity: a synthesis review. *Annals of the New York Academy of*

1053   *Sciences*, *1472*(1), 76–94. https://doi.org/10.1111/nyas.14354

1054   Yun, Y., Liu, C., Luo, Y., Liang, X., Huang, L., Chen, F., & Rasmmusen, R. (2020).

1055   Convection-permitting regional climate simulation of warm-season precipitation over

1056   Eastern China. *Climate Dynamics*, *54*(3), 1469–1489. https://doi.org/10.1007/s00382-

1057   019-05070-y

1058   Zhang, M., Xu, W., Hu, Z., Merz, C., Ma, M., Wei, J., et al. (2022). Projection of future climate

1059   change in the Poyang Lake Basin of China under the global warming of 1.5–3°C.

1060   *Frontiers in Environmental Science*, *10*. Retrieved from

1061   https://www.frontiersin.org/articles/10.3389/fenvs.2022.985145

1062   Zhang, Qi, Ye, X., Werner, A. D., Li, Y., Yao, J., Li, X., & Xu, C. (2014). An investigation of

1063   enhanced recessions in Poyang Lake: Comparison of Yangtze River and local catchment

1064   impacts. *Journal of Hydrology*, *517*, 425–434.

1065   https://doi.org/10.1016/j.jhydrol.2014.05.051

Zhang, Qiang, Liu, Y., Yang, G., & Zhang, Z. (2011). Precipitation and hydrological variations and related associations with large-scale circulation in the Poyang Lake basin, China. *Hydrological Processes*, *25*(5), 740–751. https://doi.org/10.1002/hyp.7863

Zhang, Qiang, Xiao, M., Singh, V. P., & Wang, Y. (2016). Spatiotemporal variations of temperature and precipitation extremes in the Poyang Lake basin, China. *Theoretical and Applied Climatology*. https://doi.org/10.1007/s00704-015-1470-6

Zhang, Z., Arnault, J., Wagner, S., Laux, P., & Kunstmann, H. (2019). Impact of Lateral Terrestrial Water Flow on Land-Atmosphere Interactions in the Heihe River Basin in China: Fully Coupled Modeling and Precipitation Recycling Analysis. *Journal of Geophysical Research: Atmospheres*, *124*(15), 8401–8423. https://doi.org/10.1029/2018JD030174

Zhang, Z., Arnault, J., Laux, P., Ma, N., Wei, J., & Kunstmann, H. (2021). Diurnal cycle of surface energy fluxes in high mountain terrain: High-resolution fully coupled atmosphere-hydrology modelling and impact of lateral flow. *Hydrological Processes*, *35*(12), e14454. https://doi.org/10.1002/hyp.14454

Zhang, Z., Arnault, J., Laux, P., Ma, N., Wei, J., Shang, S., & Kunstmann, H. (2022). Convection-permitting fully coupled WRF-Hydro ensemble simulations in high mountain environment: impact of boundary layer- and lateral flow parameterizations on land–atmosphere interactions. *Climate Dynamics*, *59*(5), 1355–1376. https://doi.org/10.1007/s00382-021-06044-9

Zhu, K., Xue, M., Zhou, B., Zhao, K., Sun, Z., Fu, P., et al. (2018). Evaluation of Real-Time Convection-Permitting Precipitation Forecasts in China During the 2013–2014 Summer

1088   Season. *Journal of Geophysical Research: Atmospheres*, *123*(2), 1037–1064.

1089   https://doi.org/10.1002/2017JD027445

1090

Figure 1.

Figure (a) Domain setup and terrain height [m a.s.l.]. (b) Terrain height [m a.s.l.].
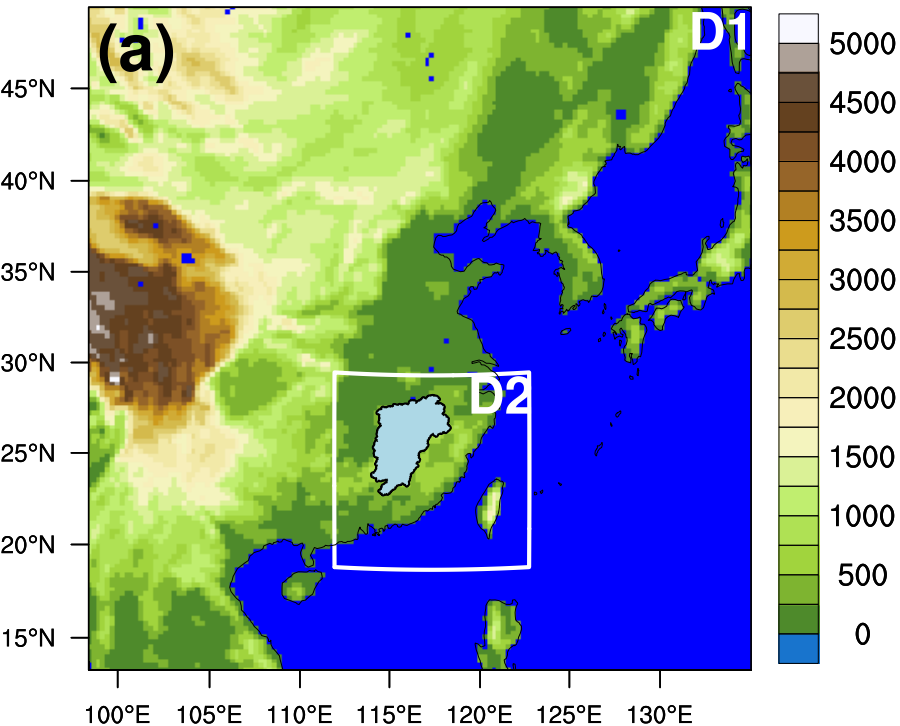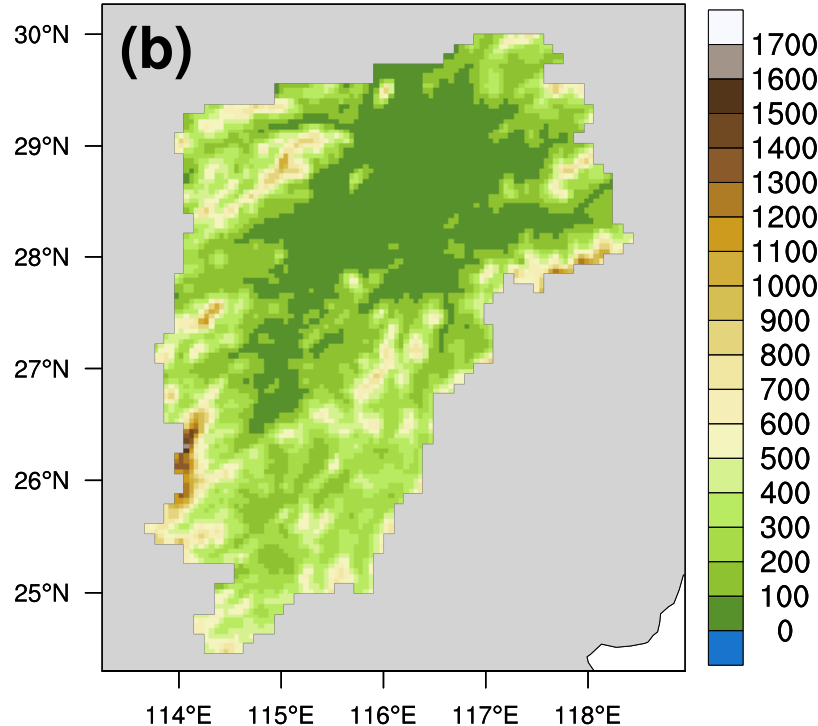
Figure 2.
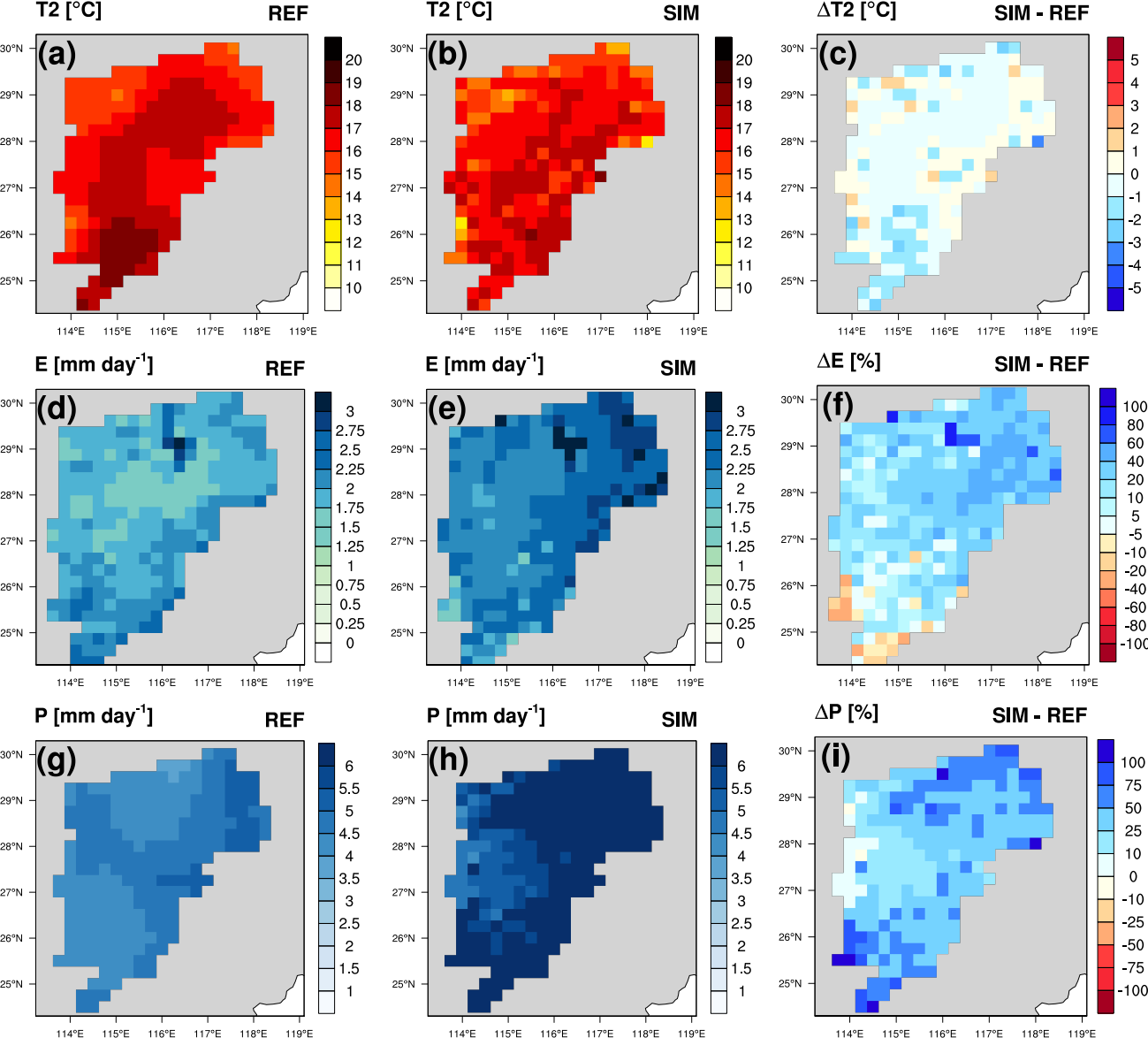
Figure 3.
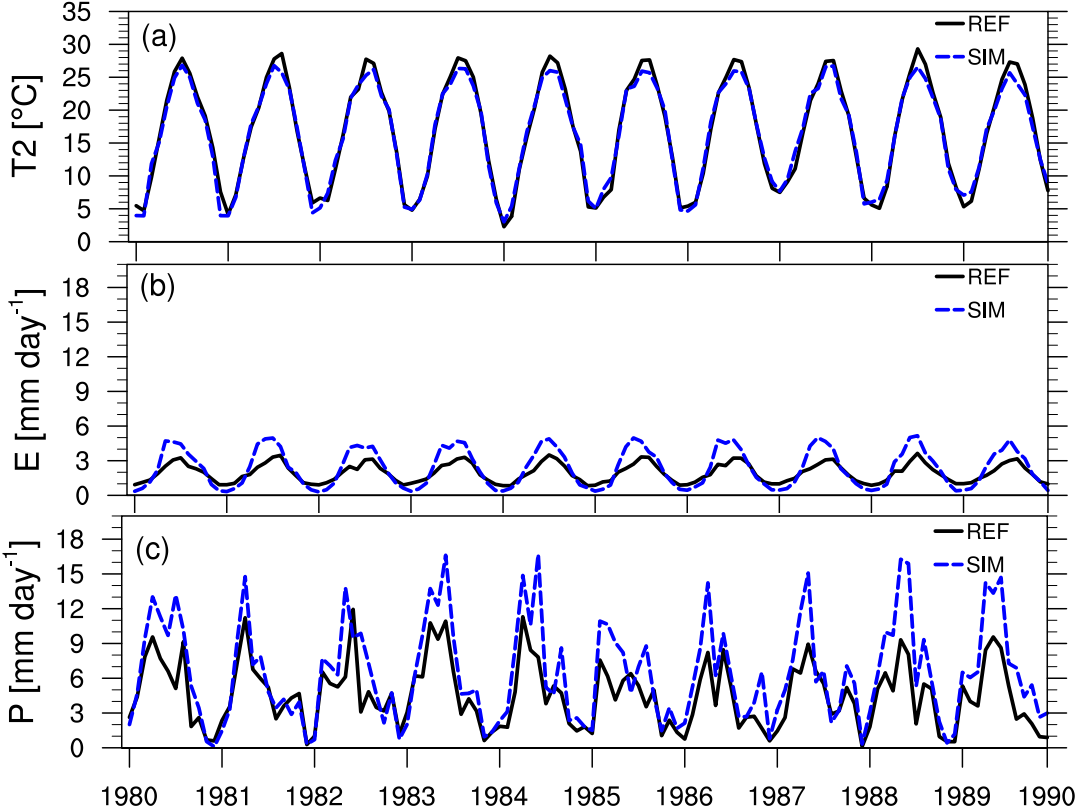
Figure 4.
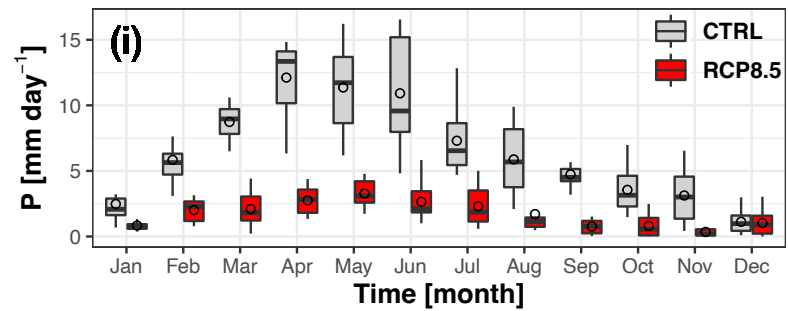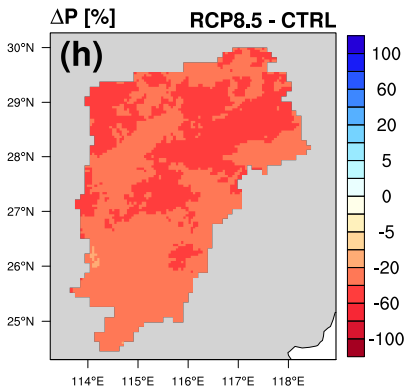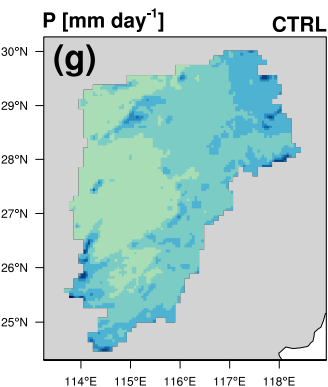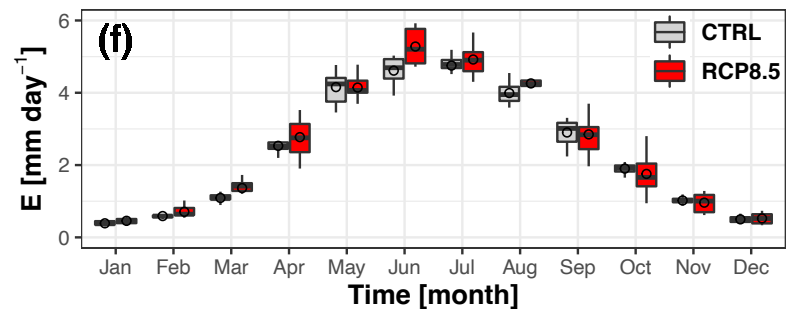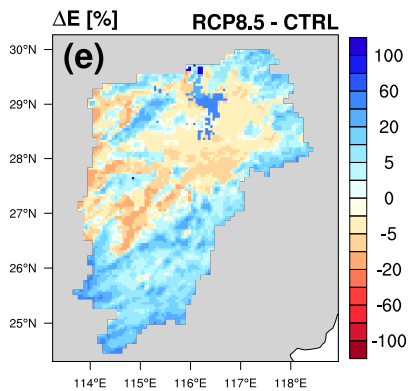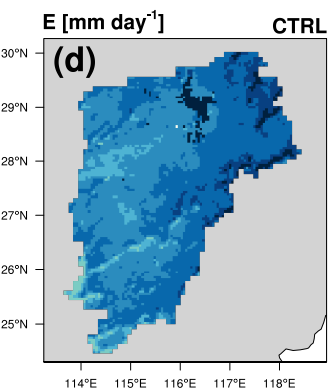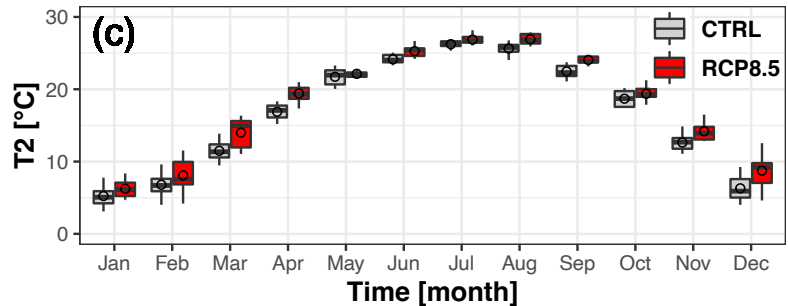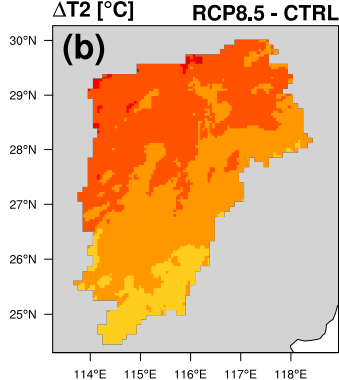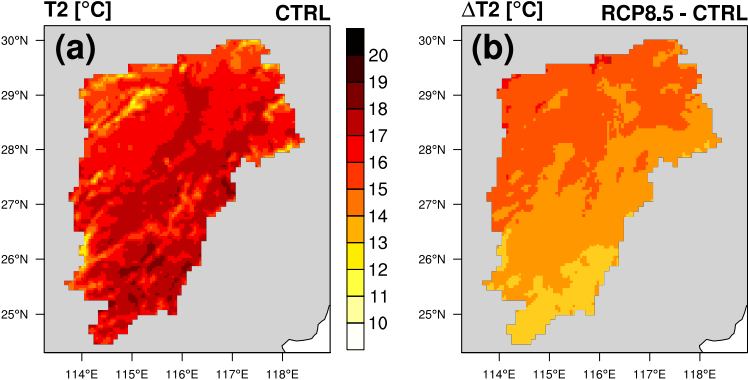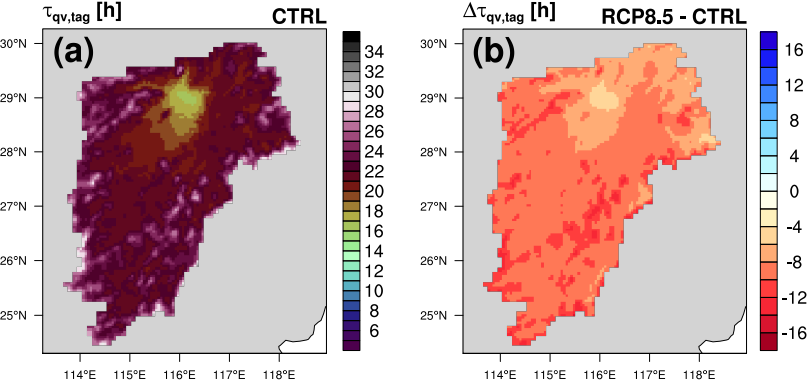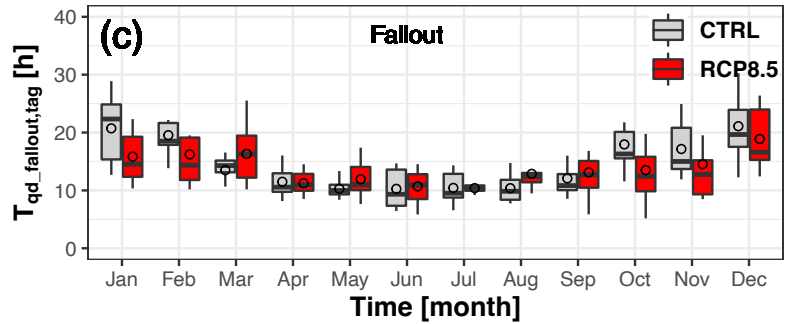
Figure 5.
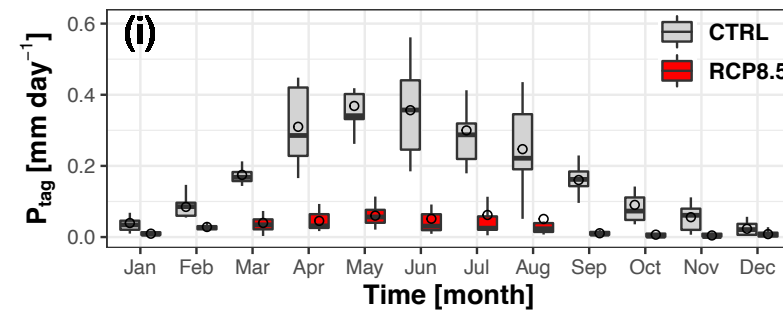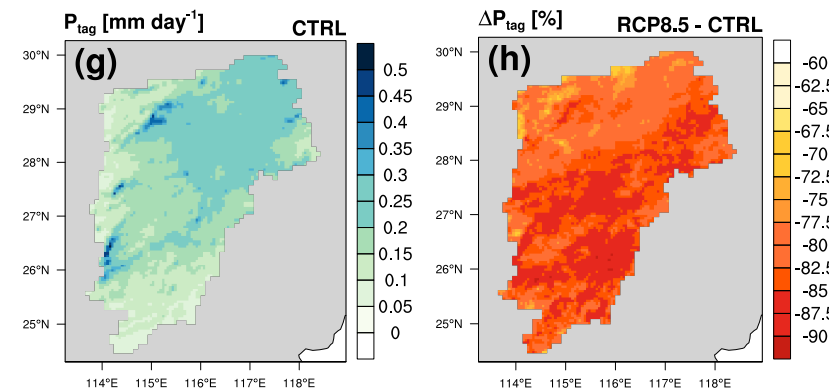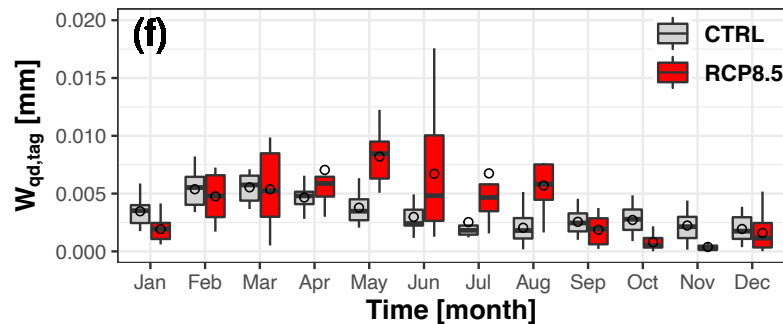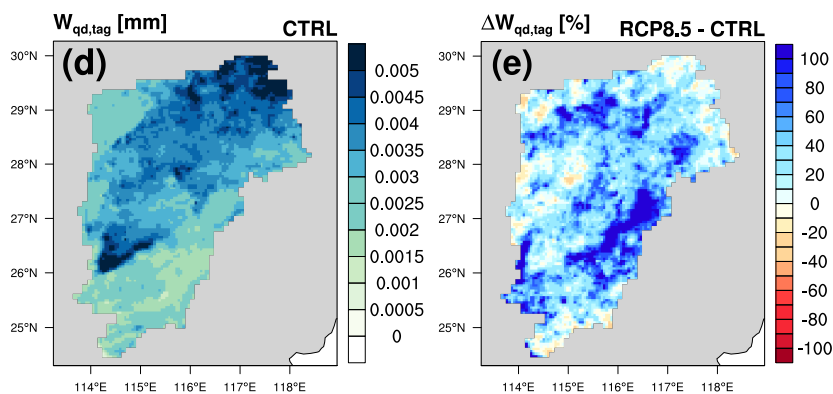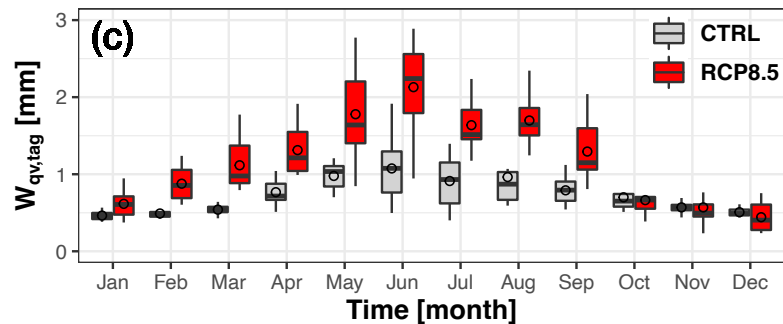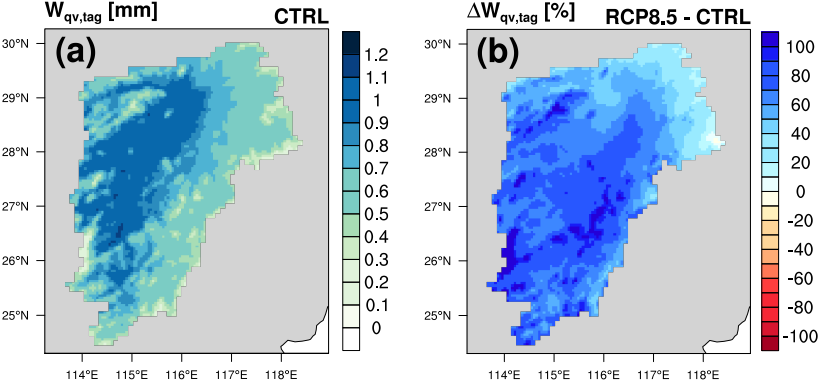
Figure 6.
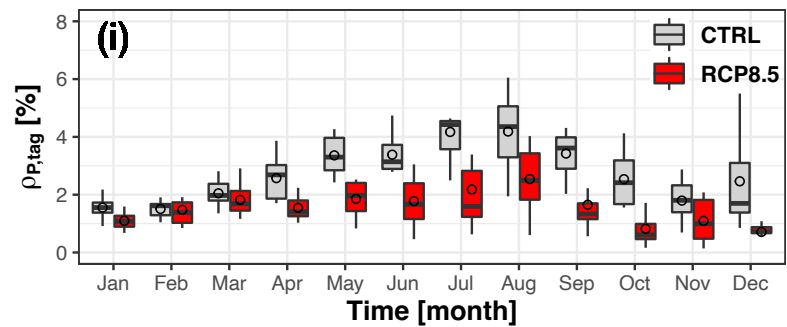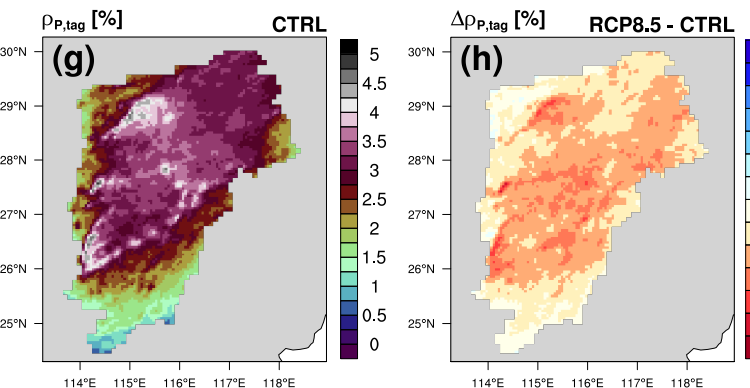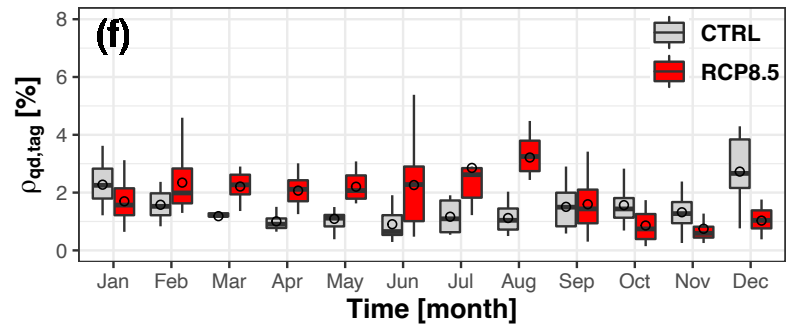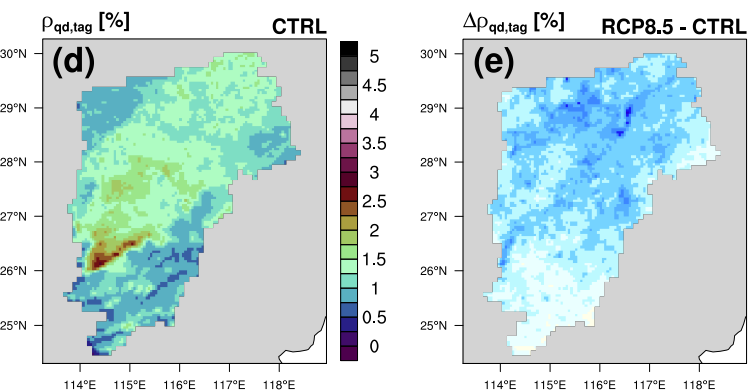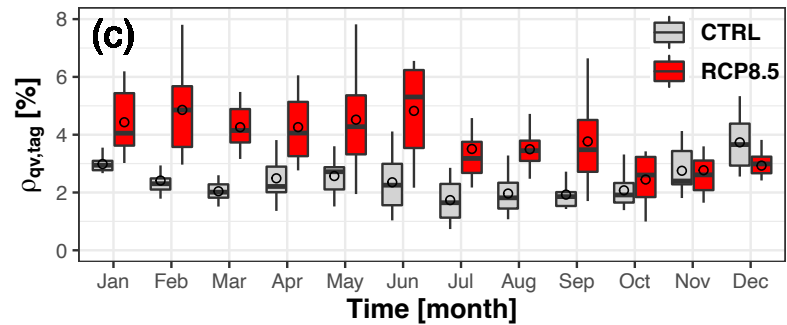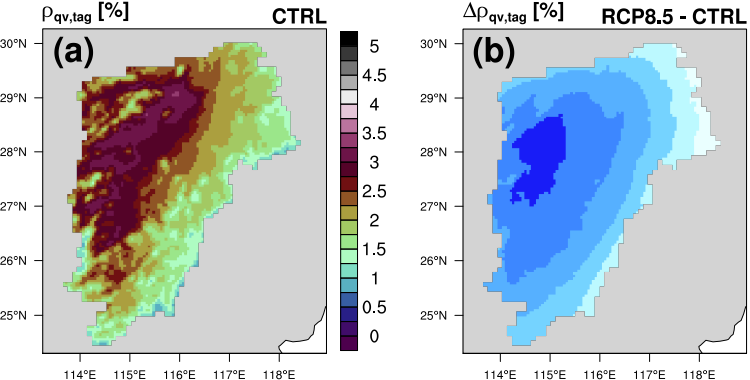
Figure 7.
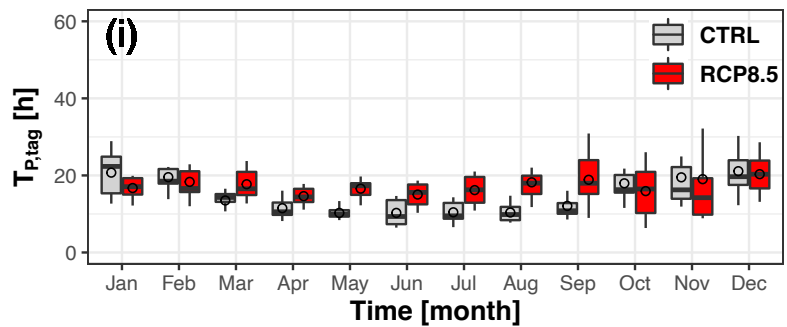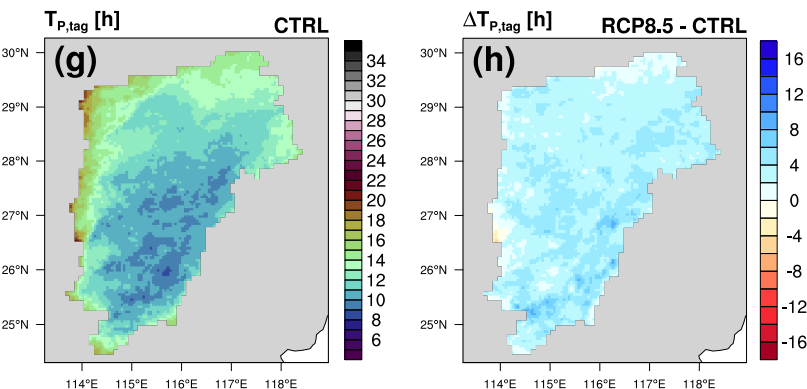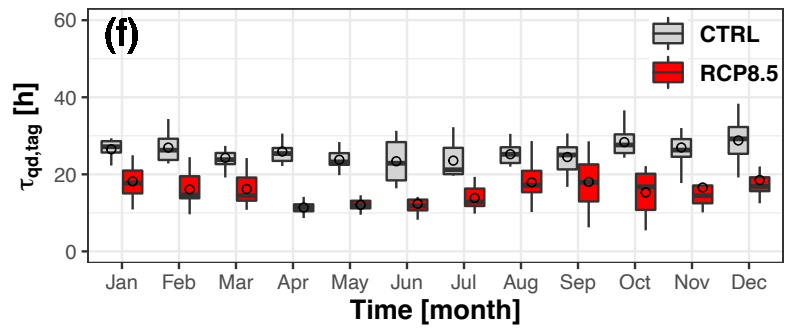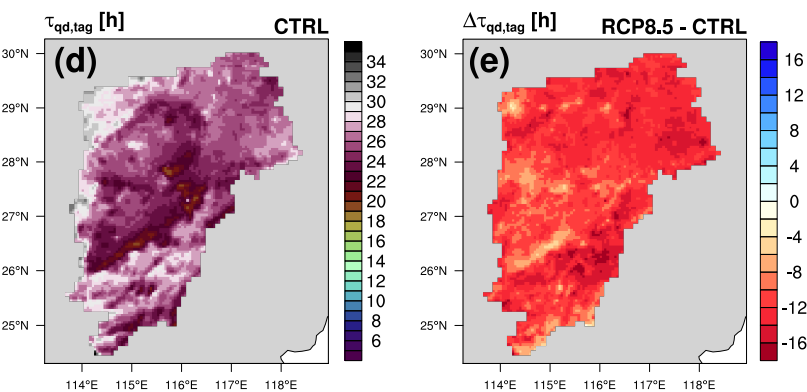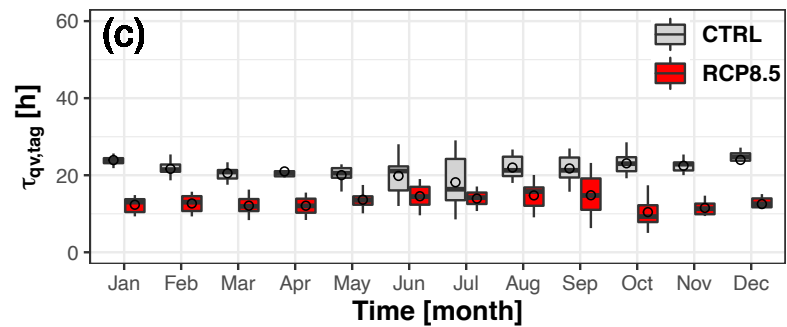
Figure 8.

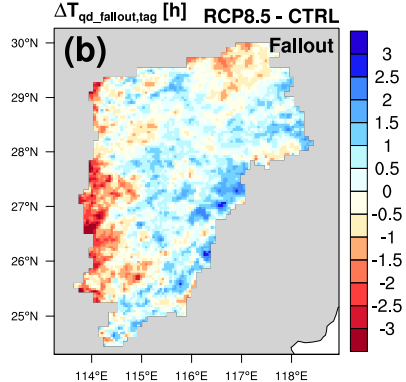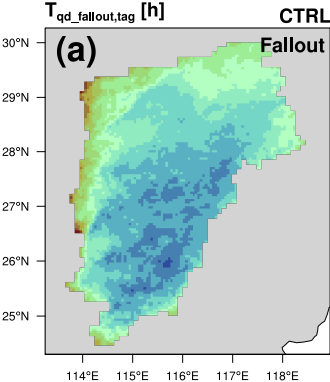1 **Figure captions**

2 **Figure 1.** (a) Model domain setup: the 30 km outer (D1) and 5 km inner (D2) WRF simulation
3 domains. The terrain heights (meters above sea level; m a.s.l.) of D1 and D2 are shown in
4 color. The light blue shaded area, i.e., the Poyang Lake basin, marks the source where
5 evaporated water is tagged and tracked using the WRF-age model. (b) Terrain height (m a.s.l.)
6 of the investigated Poyang Lake basin.

7 **Figure 2.** Spatial distributions of the reference datasets (REF, left column) and the simulated
8 (SIM, middle column) 2-meter air temperature $T2$ in °C (first row), evaporation E in mm day^{-1}
9 (second row), and precipitation P in mm day^{-1} (third row), averaged for the period 1980-1989.
10 The right column shows the corresponding differences between the simulation and the
11 reference datasets (SIM - REF).

12 **Figure 3.** Temporal variations of the basin-averaged 2-meter air temperature $T2$ (°C),
13 evaporation E (mm day^{-1}), and precipitation P (mm day^{-1}) from the reference datasets (REF,
14 black solid line) and the simulation (SIM, blue dashed line) for the period from 1980 to 1989.

15 **Figure 4.** Spatial distributions of (first row) the simulated 2-meter air temperature $T2$ in °C,
16 (second row) evaporation E in mm day^{-1}, and (third row) precipitation P in mm day^{-1} over the
17 Poyang Lake basin, averaged for (left column) the historical period 1980-1989 derived from the
18 CTRL simulation. Middle column shows the differences $\Delta T2$ (°C), ΔE (%), and ΔP (%) between
19 the future (2040-2049) RCP8.5 simulation and the historical CTRL simulation. The right
20 column shows the boxplots of monthly variations of the basin-averaged $T2$ in °C, E in mm day^{-1}
21 ^{1}, and P in mm day^{-1} from the historical CTRL (in gray) and future RCP8.5 (in red) simulations.
22 The horizonal black solid lines and the black circles indicate medium and mean, respectively.
23 The upper and bottom bounds of the box denote the 75th and 25th percentiles, respectively.
24 The upper and bottom whiskers stand for the 95th and 5th percentiles, respectively.

25 **Figure 5.** As in Figure 4, but for (top row) the column-integrated tagged water vapor $W_{qv,tag}$
26 (mm), (middle row) the column-integrated tagged condensed atmospheric moisture $W_{qd,tag}$
27 (mm), and (bottom row) the tagged precipitation P_{tag} (mm day^{-1}).

28 **Figure 6.** As in Figure 4, but for the contribution ratios for (top row) the column-integrated
29 tagged water vapor $\rho_{qv,tag}$ (%), (middle row) the column-integrated tagged condensed
30 atmospheric moisture $\rho_{qd,tag}$ (%), and (bottom row) the tagged precipitation $\rho_{P,tag}$ (%).

31 **Figure 7.** As in Figure 4, but for the atmospheric residence times of (top row) the column-
32 integrated tagged water vapor $\tau_{qv,tag}$ (h) and (middle row) the column-integrated tagged
33 condensed atmospheric moisture $\tau_{qd,tag}$ (h), and (bottom row) the atmospheric transit time of
34 the tagged precipitation $T_{P,tag}$ (h).

35

36 **Figure 8.** As in Figure 4, but for the atmospheric transit time of the tagged precipitating water
37 fallout $T_{qd\_fallout,tag}$ (h).

38

39

40 **Table 1.** Model configuration and physical schemes of the WRF-age model used in this study.

Domain name	D1	D2
	Model configuration	
Domain size (grid points)	141 × 141	247 × 247
Horizontal resolution (km)	30	5
Vertical discretization (levels)	38	38
Time step (s)	60	20
Boundary update	6-hour	3-hour
	Physical scheme	
Cumulus	BMJ	-
Shortwave radiation	Dudhia	
Longwave radiation	RRTM	
Microphysics	WSM5	
Land surface	NOAH	
Surface layer	Revised MM5 Monin-Obukhov scheme	
Planetary boundary layer	YSU	
Shallow convection	-	

41